LAWRENCE
LIVERMORE
NATIONAL
LABORATORY

UCRL-JRNL-205627

Reactive Transport Modelling of CO2 Storage in Saline Aquifers to Elucidate Fundamental Processes, Trapping Mechanisms, and Sequestration Partitioning

James W. Johnson, John J. Nitao, Kevin G. Knauss

July 29, 2004

Geological Society of London Special Publication on Carbon Sequestration Technologies

Disclaimer

Reactive transport modelling of CO_2 storage in saline aquifers to elucidate fundamental processes, trapping mechanisms, and sequestration partitioning

James W. Johnson*, John J. Nitao, and Kevin G. Knauss

Lawrence Livermore National Laboratory
Environmental Sciences Division
L-221, P.O. Box 808, Livermore, CA 94550
* Corresponding author (jwjohnson@llnl.gov)

Abstract

The ultimate fate of CO_2 injected into saline aquifers for environmental isolation is governed by three interdependent yet conceptually distinct processes: CO_2 migration as a buoyant immiscible fluid phase, direct chemical interaction of this rising plume with ambient saline waters, and its indirect chemical interaction with aquifer and cap-rock minerals through the aqueous wetting phase. Each process is directly linked to a corresponding trapping mechanism: immiscible plume migration to hydrodynamic trapping, plume-water interaction to solubility trapping, and plume-mineral interaction to mineral trapping. In this study, reactive transport modelling of CO_2 storage in a shale-capped sandstone aquifer at Sleipner has elucidated and established key parametric dependencies of these fundamental processes, the associated trapping mechanisms, and sequestration partitioning among them during consecutive 10-year prograde (active-injection) and retrograde (post-injection) regimes.

Intra-aquifer permeability structure controls the path of immiscible CO_2 migration, thereby establishing the spatial framework of plume-aquifer interaction and the *potential* effectiveness of solubility and mineral trapping. Inter-bedded thin shales—which occur at Sleipner—retard vertical and promote lateral plume migration, thereby significantly expanding this framework and enhancing this potential. *Actual* efficacy of these trapping mechanisms is determined by compositional characteristics of the aquifer and cap rock: the degree of solubility trapping decreases with increasing formation-water salinity, while that of mineral trapping is proportional to the bulk concentration of carbonate-forming elements—principally Fe, Mg, Ca, Na, and Al. In the near-field environment of Sleipner-like settings, 80-85% by mass of injected CO_2 remains and migrates as an immiscible fluid phase, 15-20% dissolves into formation waters, and less than 1% precipitates as carbonate minerals. This partitioning defines the relative effectiveness of hydrodynamic, solubility, and mineral trapping on a mass basis.

Seemingly inconsequential, mineral trapping has enormous strategic significance: it maintains injectivity, delineates the storage volume, and improves cap-rock integrity. We have identified four distinct mechanisms: dawsonite [$NaAlCO_3(OH)_2$] cementation occurs throughout the intra-aquifer plume, while calcite-group carbonates [principally, $(Fe,Mg,Ca)CO_3$] precipitate via disparate processes along lateral and upper plume margins, and by yet another process within inter-bedded and cap-rock shales. The coupled mineral dissolution/precipitation reaction associated with each mechanism reduces local porosity and permeability. For Sleipner-like

settings, the magnitude of such reduction for dawsonite cementation is near negligible; hence, this process effectively maintains initial CO_2 injectivity. Of similarly small magnitude is the reduction associated with formation of carbonate rind along upper and lateral plume boundaries; these processes effectively delineate the CO_2 storage volume, and for saline aquifers anomalously rich in Fe-Mg-Ca may partially self-seal the plume. Porosity and permeability reduction is most extreme within shales, because their clay-rich mineralogy defines bulk Fe-Mg concentrations much greater than those of saline aquifers. In the basal cap-rock shale of our models, these reductions amount to 4.5 and 13%, respectively, after the prograde regime.

During the retrograde phase, residual saturation of immiscible CO_2 maintains the prograde extent of solubility trapping while continuously enhancing that of mineral trapping. At the close of our 20-year simulations, initial porosity and permeability of the basal cap-rock shale have been reduced by 8 and 22%, respectively. Extrapolating to hypothetical complete consumption of Fe-Mg-bearing shale minerals (here, 10 vol.% Mg-chlorite) yields an ultimate reduction of about 52 and 90%, respectively, after 130 years. Hence, the most crucial strategic impact of mineral trapping in Sleipner-like settings: it continuously improves hydrodynamic seal integrity of the cap rock and, therefore, containment of the immiscible plume and solubility-trapped CO_2.

Introduction

Sufficient curbing of projected anthropogenic CO_2 emissions to achieve a stabilized "safe" atmospheric concentration ranks high among the grand challenges of this century. In the near term, significant emissions reduction can only be achieved through innovative capture/isolation strategies applied to point-source waste streams. Among currently proposed storage techniques, injection into confined geologic formations—in particular, saline aquifers, given their immense storage capacity and widespread geographic distribution—represents one of the most promising alternatives. Successful implementation of this approach hinges on our ability to predict the relative effectiveness of subsurface CO_2 migration and sequestration processes (isolation performance) as a function of key aquifer and cap-rock properties (screening criteria), which will enable us to identify optimal sites and forecast their long-term security.

Specific requirements of this predictive capability can be obtained by subdividing these competing processes into their fundamental components. In terms of migration, injected CO_2 moves by volumetric displacement of formation waters, with which it is largely immiscible; by gravity segregation, which causes the immiscible plume to rise owing to its relatively low density; and by viscous fingering, which causes it to migrate preferentially into local high-permeability zones owing to its relatively low viscosity. In terms of sequestration, some fraction of the rising plume will dissolve into formation waters (solubility trapping); some fraction will react with formation minerals to precipitate carbonates (mineral trapping); and the remaining fraction will reach and become isolated beneath the cap rock (hydrodynamic trapping), migrate up-dip along this interface, and accumulate in any local topographic highs (structural trapping). Numerical simulation of these interdependent migration and sequestration processes requires a computational capability that explicitly represents and couples multiphase

flow and kinetically controlled geochemical processes within porous media characterized by physical and compositional heterogeneity.

We have developed a unique computational package that implements this capability, and in earlier studies (Johnson et al., 2001; Johnson and Nitao, 2002) used it to address a series of key technical issues regarding CO_2 storage in saline aquifers. In these investigations, we quantified the dependence of migration/sequestration balance on permeability structure and composition, the relative effectiveness of hydrodynamic, solubility, and mineral trapping mechanisms, and the isolation performance of a typical shale cap rock. Further, we introduced the concept of prograde (active-injection) and retrograde (post-injection) storage regimes, and demonstrated that residual saturation of immiscible CO_2 during the latter maintains or enhances prograde trapping mechanisms.

In the present contribution, we first provide an overview of the reactive transport modelling approach and our simulation capabilities. We then use this methodology and computational package to elucidate and describe the fundamental processes, associated trapping mechanisms, and sequestration partitioning that characterize prograde and retrograde CO_2 storage regimes in Sleipner-like settings. Based on this description, we propose a resume of screening criteria that portend optimal isolation performance in such environments. Finally, we outline a series of important future investigations that are posed by the results of this study.

Reactive transport modelling: methodology and simulation tools

Reactive transport modelling is an advanced computational method for quantitatively predicting the long-term consequences of natural or engineered perturbations to the subsurface environment (Johnson et al., 1999). Because these predictions typically involve space, time, and system complexity scales that preclude development of direct analytical or experimental analogs, they often represent a unique forecasting tool. The necessary point of departure for predictive investigations of this kind is established by successful application of the method to simulate well-constrained laboratory experiments (e.g., Bertrand et al., 1994; Johnson et al., 1998).

The approach is based upon mathematical models of the integrated thermal, hydrological, geochemical, and geomechanical processes that redistribute mass and energy in response to the disequilibrium state imposed by perturbations such as magmatic intrusion or CO_2 injection (Figure 1). Traditionally, such models have been developed as separate entities and applied as such to address specific issues relevant their individual scope. The fundamental advance embodied in reactive transport modelling is its *explicit integration* of these conceptually distinct process models.

Translating the theoretical framework of this methodology into a state-of-the-art reactive transport simulator requires implementing robust numerical methods that approximate and discretize the coupled mathematical models, while encoding these numerical representations in the form of efficient software designed to exploit advanced parallel architectures. On the pre-

processing end, the simulator must be supported by geochemical software and databases, which together provide the requisite equilibrium reference frame and kinetic parameters for application-specific sets of chemical species. On the post-processing end, it must interface smoothly with a versatile graphics utility, which facilitates visualization of myriad results. We have developed a unique computational package that integrates these three essential elements: a state-of-the–art reactive transport simulator (NUFT), supporting geochemical software and databases (GEMBOCHS), and a dedicated graphics package (Xtool: Daveler, 1998).

NUFT (Nitao, 1998a,b) is a software package that facilitates numerical simulation of non-isothermal multiphase/multicomponent flow and reactive transport within a wide range of subsurface environments characterized by multi-scale physical and compositional heterogeneity. The package implements an integrated finite-difference, spatial discretization to solve the flow and reactive-transport equations, using the Newton-Raphson method to solve the resulting nonlinear systems at each time step. Explicit account is taken of multiphase advection, diffusion, and dispersion; of relative permeability and capillary pressure, using an extended Van Genuchten formulation (Parker et al., 1987); and of kinetically controlled fluid-mineral reactions, using rate laws from transition state theory (e.g., Lasaga, 1998). Moreover, explicit account is also taken of *coupling between* these transport and geochemical processes through the dependence of permeability on porosity changes due to mineral precipitation/dissolution, using a normalized Kozeny equation (Scheidegger, 1974), and through the dependence of fluid-phase volumetric saturations on gas (e.g., $CO_2(g)$) generated or consumed by fluid-mineral reactions.

The equation-of-state and viscosity formulations implemented in NUFT for supercritical CO_2 are those developed by Span and Wagner (1996) and Fenghour and Wakeman (1998), respectively. The corresponding formulations implemented for H_2O are those presented by Meyer et al. (1993). Chemical interaction between and within distinct fluid phases is governed by inter- and intra-phase equilibrium constraints. Activity coefficients for charged aqueous solutes are represented using an extended form of the Debye-Huckel equation (B-dot formulation: Helgeson, 1969), those for non-polar neutral solutes are represented using the Drummond (1981) model, and those for polar neutral solutes are taken to be unity.

The GEMBOCHS system (Johnson and Lundeen, 1994a,b, 1995) integrates a comprehensive relational thermodynamic/kinetic database and dedicated software library that together facilitate generation of application-specific thermodynamic/kinetic datafiles for use with a variety of geochemical modelling codes and reactive transport simulators. The thermodynamic database covers about 3200 distinct chemical species, spanning 86 elements of the periodic table; its core component is the current version of the SUPCRT92 database (Johnson et al., 1992; Shock, 1998), which covers about 1550 species, spanning 82 elements. Custom datafiles are generated using Jewel, a GUI-driven software package that extrapolates reference-state properties to elevated P-T conditions using a number of standard algorithms, the core set of which are those encoded with the SUPCRT92 software package (Johnson et al., 1992). These include global- and
critical-region equations of state and a dielectric formulation for H_2O (Johnson and Norton, 1991) that are explicitly integrated with equations of state for both aqueous solutes (Tanger and

Helgeson, 1988; Shock et al., 1992) and minerals/gases (Helgeson et al., 1978).

CO_2 storage at Sleipner: overview and model definition

Statoil's North-Sea Sleipner facility is the world's first saline-aquifer CO_2 storage site. Here, excess CO_2 from a natural-gas production stream is removed by amine absorption, then stripped from the amine, and subsequently injected into the Utsira formation 1000 m below the seabed for the purpose of environmental isolation (Gregersen et al., 1998). Since October 1996, this process has diverted from atmospheric release roughly one million tons of CO_2 annually.

At Sleipner, the CO_2 injection well extends 3-4 km horizontally before reaching the expulsion zone—a screen length of 100 m near the base of the Utsira. As a result of this lengthy transport, the thermal perturbation associated with CO_2 injection is negligible. In addition, the 200-m-thick Utsira is laterally extensive and consists of extremely permeable unconsolidated sandstone, capped by the several-100 m thick Nordland shale. As a consequence, CO_2 injectivity is high and injection-induced pressure anomalies along the cap-rock interface are minimal. Hence, at Sleipner thermal and geomechanical processes represent second-order effects, while interdependent multiphase flow and geochemical processes dominate integrated system response to the perturbation event.

Numerical simulation of this scenario—which typifies desirable saline-aquifer storage sites—involves constructing representative spatial domains, assigning to these the appropriate initial and boundary conditions based on hydrologic and compositional data, and compiling the thermodynamic and kinetic data required to represent compositional evolution of the system.

Simulation domains XSH, CSH, and DSH

In this study, all of the reactive transport simulations are conducted within a single spatial domain, which represents the near-field environment of CO_2 disposal at Sleipner (Figure 2A), and over a single time frame, which encompasses equal-duration prograde and retrograde regimes. In the common physical setting, an Utsira-like saline aquifer (200-m thick) is confined by a shale cap rock (25 m), which itself is overlain by a thin confined saline aquifer (25 m) to facilitate evaluation of cap-rock performance. In the common 20-year time frame, an injection rate of 10,000 tons-CO_2/yr is first maintained for 10 years (prograde regime), then ramped down to zero over three months (prograde-retrograde transition phase), and finally maintained at zero for another 9.75 years (retrograde regime). This spatial domain and injection rate correspond to a one-meter-thick cross-section through and perpendicular to the actual 100-m screen length of CO_2 injection at Sleipner.

Within this domain, three distinct injection scenarios—models XSH, CSH, and DSH—are evaluated. Model XSH (Figure 2B) examines CO_2 injection into a shale-capped homogeneous sandstone aquifer. Models CSH and DSH impose into XSH four thin (3-m-thick) intra-aquifer shales, which are separated from the cap rock and each other by 25 m. Model CSH (Figure 2C)

examines the effect of imposing laterally-continuous microfractured shales, whose assigned permeability (3 mD) equates to a continuum representation of 100-μm fractures spaced roughly 30 m apart. Model DSH (Figure 2D) examines the effect of imposing laterally-discontinuous shales, which are bridged by lateral facies change to sandstone; assigned permeability of these shales (3 μD; same as the cap rock) reflects typical shale integrity (Freeze and Cherry, 1979).

Each model contains about 4000 variably sized grid cells, which range in width-by-height from 0.5-by-1.0 m for the injection well to 25-by-5 m near lateral boundaries. The base and top of the domains are impermeable to fluid flow and mass transfer. Constant hydrostatic head and geochemical conditions are maintained within a column of vanishingly thin lateral boundary cells, which therefore serve as an infinite sink for outward migration of both immiscible CO_2 and aqueous phases; i.e., lateral domain boundaries can be viewed as permeable to outward fluid flow and mass transfer. An ambient flow field has not been imposed within the saline aquifer, nor has any degree of tilt or non-planar topography been imposed on the aquifer-cap rock interface.

Hydrologic and compositional data

Pressure-temperature conditions, porosities, and permeabilities assigned to the saline aquifer are consistent with those reported for the Utsira formation; such data are presently unavailable for inter-bedded and cap-rock shales at Sleipner, and have been estimated (Table 1). Compositional data adopted for the saline aquifer are based on mineralogy reported for a representative North Sea formation (Table 2), which specifies an impure quartz sand, and a fluid analysis reported for the Utsira itself 200 km north of Sleipner at Oseberg, which defines a seawater-like aqueous phase (Table 3). Analogous data for inter-bedded and cap-rock shales directly representative of those at Sleipner are currently unavailable; these units have been assigned an average shale mineralogy (Table 2) and a fluid composition identical to that of the saline aquifer (Table 3).

Our approach of incorporating Fe-Mg solid solutions as representative Mg end-member components (Table 2) reflects the necessity of removing O_2(aq) and total Fe from the fluid analysis (see Table 3 footnotes). Note that within the system Fe-C-O-H for the P-T conditions and injection CO_2 fugacity at Sleipner (see below), siderite is stable over a wide range of O_2(g) fugacity—from the lower limit of H_2O stability ($10^{-83.2}$) to hematite-siderite equilibrium ($10^{-52.7}$)—roughly centered about the magnetite-hematite buffer ($10^{-69.0}$). Hence, incorporating Fe-Mg solid solutions as Fe end-member components would have little effect on the present study beyond replacing magnesite [$MgCO_3$] with siderite [$FeCO_3$] as the relevant calcite-group carbonate. In all likelihood, reality lies within the middle ground of siderite-magnesite solid solutions.

The minor calcite fraction (5%) reported for the Utsira proxy (Table 2) was excluded in the simulations because the actual Utsira formation is distinctly unconsolidated (Gregersen et al., 1998), which reflects a lack of carbonate cement, while the adopted shale mineralogy excludes carbonates because this constraint is most typical of such lithologies (Blatt et al., 1972). Further, in the context of the present modelling work, it is advantageous to restrict mineral-trapped CO_2

to the form of injection-triggered carbonate precipitation, which simplifies account of sequestration partitioning into mineral-trapping mechanisms. These first-order approximations are made while recognizing that many uncemented sandstones do contain small fractions of clastic or biogenic calcite, carbonaceous shales are far from uncommon, and that these complications need be addressed in future work.

The adopted waste stream composition is pure CO_2, and it is injected under supercritical conditions (37°C, 110.5 bars) at the base of the saline aquifer. At this pressure and temperature, the injection CO_2 fugacity is 61.05 bars in the context of the adopted CO_2 fugacity coefficient (see below). Although aqueous solute concentrations are explicitly accounted for (Table 3), PVT properties of the aqueous phase are here taken to be those of pure H_2O instead of an actual seawater-like fluid in the absence (ambient conditions) or equilibrated presence (prograde/ retrograde regimes) of an immiscible CO_2 phase. At the relevant P-T conditions, density differences introduced by this approximation are less than 3% with respect to pure seawater (Fofonoff and Millard, 1983), and less than 4% with respect to seawater equilibrated with immiscible CO_2 (Ennis-King and Paterson, 2003). Hence, this simplification has near-negligible impact on prograde buoyancy-driven immiscible CO_2 migration (and dependent aqueous flow), where the density contrast between immiscible CO_2 and aqueous phases is 30-40%. However, it could be significant during the retrograde phase, when aqueous convection may be governed by very small density contrasts (on the order of 1%) between aqueous phases that are and are not equilibrated with residual immiscible CO_2 (Ennis-King and Paterson, 2002, 2003; Lindeberg and Bergmo, 2002).

As is appropriate, the aqueous phase is taken to be the wetting fluid. Hence, chemical interaction of the immiscible CO_2 fluid and kinetically-reacting mineral grains occurs exclusively through a grain-surrounding aqueous-phase film, whose thickness decreases with increasing immiscible CO_2 saturation. The residual saturation of immiscible CO_2—the limit below which it is no longer a contiguous (advectively mobile) phase—is taken to be 0.05, which falls at the low end of values reported for various sandstones (Holtz, 2002, 2003). Irreducible water saturation is taken to be 0.20. Adopted Van Genuchten parameters are as follows: *m* (sorting parameter) is taken to be 0.4 (moderately well sorted) for both sandstone and shale, while α (inversely proportional to bubble pressure) is taken to be 66 and 0.18 $bars^{-1}$ for sandstone and shale, respectively.

Thermodynamic and kinetic data

Equilibrium thermodynamic characterization of the adopted compositional framework (Tables 2-3) is specified within a data file for the 10-component system K-Na-Ca-Mg-Al-Si-C-O-H-Cl that includes hydrolysis constants for 36 aqueous solutes, 2 gases, and 70 minerals at 100 bars and 20-90°C. This equilibrium reference frame is derived almost entirely from those data—and using exclusively those equations of state—contained in the SUPCRT92 software package (Johnson et al., 1992; Shock, 1998). Adopted thermodynamic data beyond those contained in SUPCRT92 include Debye-Huckel ion-size parameters for aqueous solutes (Johnson and Lundeen, 1994b), a fugacity coefficient (0.55) for CO_2(g) (Garrels and Christ, 1965), and

reference-state properties for dawsonite (Robie et al., 1978). In addition, data for three plagioclase solid-solution compositions (plag-Ab80, plag-Ab50, plag-Ab20) were incorporated; these were derived using an ideal site-mixing model applied to SUPCRT92 data for albite and anorthite. Finally, dolomite and antigorite were suppressed from precipitating, owing to the well known (but poorly quantified) extreme discrepancy between low-temperature dissolution and precipitation rates of the former (e.g., Berner, 1971), and problematic stoichiometry of the latter.

Requisite kinetic data are also specified within the data file; specifically, reference-state mineral dissolution and precipitation rate constants, activation energies, and reactive specific surface areas (Table 4). In general, these parameters are markedly less certain than the related thermodynamic data. The reactive specific surface area of dissolving and precipitating minerals in the subsurface is a particularly important parameter that is poorly quantified at present. Here, the following approach has been used to assign values to this key variable. First, the specific surface area is calculated for spherical grains of the relevant size fraction, presuming the nominal grain diameter is equivalent for all minerals within a given lithology. Adopted diameters are 0.25 mm for the saline aquifer and 0.025 mm for the shales (Table 2); hence, idealized specific surface areas are ten times larger in the shales than in the aquifer. These idealized values are then multiplied by a scaling factor derived from experimentally observed factors of increase between specific surface areas of 100-μm spheres and BET-measured specific surface areas of 100-μm grains for quartz, albite, anorthite, K-feldspar, and muscovite (Table 4). Scaling factors for primary minerals outside this group are assigned based on closest structural analogy.

In the highly porous and permeable saline aquifer, all of the mineral surface area is considered to be available reactive surface area; i.e., in contact with the aqueous phase. However, within typical shales only a small fraction of the total mineral surface area is in such contact; specifically, those grain surfaces along and within diffusion distance of fracture walls. As a first approximation, this reactive fraction of the total surface area is taken to be 10%. Because the specific surface area of shales was taken to be 10 times that characterizing the aquifer, *in this continuum model reactive specific surface area in the shales and aquifer is identical* (Table 4). For precipitation of secondary minerals in both the aquifer and shales, all reactive surface area of primary minerals is considered to represent available substrate; i.e., 100% and 10% of the *total* surface area per bulk volume for the aquifer and shales, respectively.

Within the adopted implementation of transition state theory rate laws, mineral dissolution and precipitation rate constants are assigned equivalent absolute magnitude, precipitation onset does not require any degree of aqueous-phase supersaturation, and the potential limiting effect of armoring on precipitation is not represented. These common approximations, taken together with the foregoing description of reactive specific surface areas, provide a first-order estimate of mineral trapping effectiveness that likely falls near the high end of reality.

Fundamental processes and associated trapping mechanisms

The ultimate fate of CO_2 injected into saline aquifers for environmental isolation is governed by three interdependent yet conceptually distinct processes: CO_2 migration as a buoyant immiscible

fluid phase, direct chemical interaction of this rising plume with ambient saline waters, and its indirect interaction with aquifer and cap-rock minerals through the aqueous phase. The first process is directly linked to hydrodynamic trapping, the second to solubility trapping and pH evolution, and the third to mineral trapping (and pH evolution). In this section, we quantify and compare the relative effectiveness of these three trapping mechanisms for models XSH, CSH, and DSH during prograde and retrograde CO_2 storage.

CO_2 immiscible migration and hydrodynamic trapping

During prograde storage, initial ascent of the immiscible CO_2 plume towards the cap rock is governed by four constraints. The first two—density contrast between CO_2 and formation waters and the absolute formation permeability—effectively determine the injection overpressure required to acheive a given influx rate, which eventually translates to a corresponding pressure anomaly along the cap-rock interface. In model XSH, the injection-point density contrast is only about 30%, but permeability is extremely high (3 Darcy); hence, injection overpressure amounts to less than one bar. The second pair of constraints—saturation-dependent relative permeability of the formation to immiscible CO_2 and pressure-dependent volumetric expansion of this phase during ascent—effectively controls dynamic plume configuration, causing concomitant lateral telescoping of its main conduit and lateral expansion of its leading edge (Figure 3A: 2.4-, 6.8-, and 12-day insets). Interplay of these two processes creates a zone of prograde residual CO_2 immiscible saturation, which marks the wake of initial plume ascent.

In model XSH, immiscible CO_2 reaches the cap rock and lateral domain boundaries within 15 and 50 days, respectively. The plume cap, column, and prograde residual saturation zones all attain near steady-state geometric plume configuration within one year (Figure 3A). At this time, CO_2 saturation has reached 0.50-0.58 within the uppermost 25 m of the aquifer (plume cap), while in the plume column it increases from 0.13 just below the cap to 0.22 at 25 m above the injection well. Hence, a steep vertical gradient connects distinct saturation profiles in the plume cap and column. Subsequent prograde evolution of CO_2 saturation is limited to a gradual increase in the plume cap, from 0.50-0.58 at one year to 0.60-0.67 after 10 years (Figure 3B).

Owing to 18% specific-volume expansion of the immiscible CO_2 fluid as it rises 200 m in the aquifer (20-bar pressure drop), once steady-state geometric configuration of the plume is attained, the intra-plume aqueous phase is displaced primarily downward within and slightly outward from the plume column and cap during prograde storage (Figure 3B). Velocities of this injection-induced aqueous flow are 15-575 cm/yr at one year, with maximum values localized within the lower two-thirds of the plume cap. The maximum values decrease with time to 110 cm/yr at two years, 40 cm/yr at five years, and 20 cm/yr at ten years. Such velocities are on the order of those typically encountered in unperturbed saline aquifers.

Just nine months into the retrograde phase, continued upward and outward plume migration has reduced the plume cap to a new steady-state thickness of 5 m (single horizontal layer of domain cells), within which CO_2 saturation has dropped to 0.52 (Figure 3C). This thin veneer now caps

a zone of uniform residual saturation that encompasses the prograde plume column and residual saturation zones. During the retrograde regime, aqueous-phase flow is directly opposite to that of the prograde regime—now primarily upward and slightly inward within the relict plume as the aqueous phase migrates into the void left by rising CO_2—while flow velocities are similar in absolute magnitude. Ten years into the retrograde phase, plume-cap saturation has diminished to 0.15 (Figure 3D).

During the prograde regime of model XSH, roughly 85% by mass of injected CO_2 remains and migrates as an immiscible fluid phase. Hence, gravity segregation is the dominant migration process and hydrodynamic trapping represents the most important potential trapping mechanism. In this model, the 25-m (3 μd) shale cap rock provides a very secure seal. In particular, CO_2 does not migrate completely through the 5 horizontal layers of 5-m-thick shale grid cells. Within the uppermost 20 m of shale, the maximum CO_2 saturation attained varies from 0.000015 in the upper 5 m to 0.0001 in the lowest 5 m—and saturation is declining at 20 years. In the 5 m of shale immediately overlying the aquifer, maximum saturation of 0.047 (less than the residual limit of 0.05) is attained at 14 years—and declines thereafter to 0.042 at 20 years. Hence, the 20-year isolation performance of this shale cap rock is both excellent and improving with time.

The presence of thin intra-aquifer shales has a profound influence on immiscible-plume migration and dependent sequestration mechanisms. For the case of laterally continuous microfractured shales (model CSH), the most obvious—and significant—effects are vertical bifurcation of the plume cap and a tremendous resultant increase in the spatial extent of plume-aquifer interaction (Figure 4A-B), which greatly enhances the potential effectiveness of solubility and mineral trapping. When laterally-discontinuous tight shales are imposed (model DSH), these effects are somewhat less pronounced; however, the lateral breaks lead to spatial recursion of focused vertical CO_2 migration paths and *lateral* saturation gradients throughout the near-field domain (Figure 4C-D), further enhancing the potential effectiveness of mineral trapping.

In model CSH, maximum steady-state CO_2 saturation *within* the four relatively permeable intra-aquifer shales (from 0.42 in the lowest to 0.25 in the highest) is attained within 5-6 years during prograde storage. During the first year of the retrograde regime, saturation within all four decreases to the residual limit of 0.05, and by 18 years has been reduced to zero (Figure 4B). In model DSH, saturation in the four relatively impermeable shales increases slowly throughout the prograde regime (reaching maximum values of 0.06-0.10). It then decreases slowly throughout the retrograde phase, eventually reaching zero at 18 years (Figure 4D). Ultimate depletion of immiscible CO_2 in the intra-aquifer shales of CSH and DSH reflects its eventual consumption by carbonate-precipitating fluid-mineral reactions (described below).

CO_2 saturation profiles for models XSH, CSH, and DSH at 3 years are shown together with the 3-year seismic profile of immiscible CO_2 accumulations at Sleipner in Figure 5. Comparison of these four images strongly suggests the presence of thin intra-aquifer shales in the upper half of Utsira Formation. Moreover, close correspondence of model CSH and the seismic data suggests that these shales are predominantly contiguous laterally and have microfracture permeability on

the order of CSH values (3 mD). The presence of lateral facies changes to sand would result in a much greater proportion of injected CO_2 reaching the cap rock after 3 years, as in model DSH, where the lateral breaks are quite restricted (10-25 m in width) relative to typical field settings.

Solubility trapping and pH evolution

Chemical interaction of the immiscible CO_2 plume with saline formation waters causes a dramatic increase in total aqueous carbon concentration, primarily as CO_2(aq) and HCO_3^-, and a substantial decrease in pH. The coupled reaction can be expressed as:

$$CO_2(g) + H_2O \leftrightarrow CO_2(aq) + H_2O \leftrightarrow HCO_3^- + H^+ \quad . \qquad (1)$$

In model XSH, formation waters equilibrate on contact with the ascending CO_2 plume, creating a coincident zone of solubility-trapped CO_2. For the adopted aqueous-phase composition (Table 3), injection CO_2(g) fugacity, and vertical pressure gradient, the CO_2 aqueous solubility limit varies from about 1.2 molal near the injection well to about 1.1 molal at the aquifer-cap rock interface (Figure 6A), accounting for roughly 15% of injected CO_2 mass within the near-field environment. This solubility limit will decrease with increasing ionic strength, owing to the "salting-out-effect" (Garrels and Christ, 1965). Hence, the effectiveness of solubility trapping will decrease with increasing formation water salinity; this compositional dependence is accounted for in simulation studies by adoption of an appropriate activity-coefficient model for dissolved-gas aqueous solutes (e.g., Drummond, 1981).

Because solubility-limited CO_2 aqueous concentration is maintained by the presence of CO_2(g), the composition-dependent degree of solubility trapping is sustained throughout the prograde regime (Figure 6A-B) by continuous CO_2 injection (Figure 3A-B) *and maintained during the retrograde phase* (Figure 6C) *by residual CO_2 saturation* (Figure 3C-D).

The presence of intra-aquifer shales retards vertical and promotes lateral migration of the immiscible CO_2 plume, thereby expanding the spatial extent of plume-aquifer interaction and reducing volume averaged CO_2 saturation within the near-field environment. The expanded interaction volume increases the total mass of CO_2 trapped within the near-field aqueous phase, while the reduced average saturation increases the mass so trapped per mass of immiscible CO_2, increasing the relative effectiveness of solubility trapping. In models CSH and DSH, the total mass of solubility-trapped CO_2 exceeds that for model XSH by a factor of 3.2 and 1.4, respectively, which is equivalent to the factor-of-increase in spatial extent of the solubility-limit CO_2 aqueous concentration (cf. Figures 6B-C and 7A-D). The mass ratio of solubility-trapped to immiscible CO_2 in models CSH and DSH exceeds that of XSH by 32 and 44%, respectively, which increases sequestration partitioning into the aqueous phase from 15 to 17 and 19%, respectively.

CO_2 aqueous concentration has dropped below even the ambient value within all intra-aquifer shales of CHS and DSH 10 years into the retrograde regime (Figures 7B,D). This reflects complete consumption of CO_2 from the intra-plume aqueous phase (and therefore from the

immiscible plume itself) by carbonate-precipitating fluid-mineral reactions.

Intra-plume pH evolution is governed by two opposing processes: aqueous solubility of CO_2(g), which dramatically decreases pH, and dependent kinetic dissolution of silicate minerals, which increases it. CO_2(g) solubility lowers pH from the ambient value of 7.1 to about 3.4 upon initial plume-formation water contact, while resultant initial silicate dissolution increases pH to roughly 4.5 throughout the plume by the time its steady-state configuration is attained (figure 6D). Continued silicate dissolution throughout the prograde regime affects continued increase in pH from 4.5 to 4.9 in the plume column and residual saturation zone, and from 4.5 to 5.2 in the plume cap (Figure 6E). During the retrograde phase, residual CO_2 saturation maintains the solubility-induced background pH, which continues to drive silicate dissolution, which in turn causes further pH increase, to about 5.3 throughout the relict plume at 20 years (Figure 6F).

The presence of intra-aquifer shales has two important effects on aquifer pH distribution and dependent mineral trapping mechanisms. First, the expanded region of low-pH fluids (Figure 7E-H) and silicate minerals under acid attack represents a similarly expanded source region of potential carbonate-forming cations. Second, spatial recursion of focused vertical CO_2 migration paths in model DSH leads to similar recursion of steep lateral gradients in pH (Figures 7C-D,G-H), which play an important role in mineral trapping.

The relatively high pH values observed within intra-aquifer shales of CSH and DSH after 20 years (Figures 7F and 7H) obtain rapidly between 16 and 18 years as the final vestige of CO_2 is consumed by local carbonate precipitation.

<u>Mineral Trapping</u>

In saline aquifers, mineral trapping will occur primarily in the form of dawsonite [$NaAlCO_3(OH)_2$] and the calcite-group carbonates, most significantly siderite [$FeCO_3$], magnesite [$MgCO_3$], calcite [$CaCO_3$], and their solid solutions. In the present models, we evaluate the contributions of dawsonite, magnesite (representing siderite-magnesite solutions), and calcite, which precipitate by four distinct mechanisms: dawsonite cementation occurs throughout the intra-aquifer plume, while magnesite and calcite precipitate via disparate processes along lateral and upper plume margins, and by yet another process within inter-bedded and cap-rock shales.

<u>Intra-plume dawsonite cementation</u>

Dawsonite precipitation results from high ambient Na and injection-induced CO_2 concentrations in the aqueous phase together with acid-induced kinetic dissolution of K-feldspar. The coupled reaction (in both the aquifer and shale environments) can be expressed as:

$$\underset{\text{K-feldspar}}{\underline{KAlSi_3O_8}} + Na^+ + CO_2(aq) + H_2O \leftrightarrows \underset{\text{dawsonite}}{\underline{NaAlCO_3(OH)_2}} + 3\,\underset{\text{qtz/chal/crist}}{\underline{SiO_2}} + K^+ \quad . \quad (2)$$

The adopted reference-state dissolution rate constant of K-feldspar is 10^3 times slower than the

dawsonite precipitation rate constant, but exceeds by a factor of 10^3-10^4 the precipitation rate constants of the three most stable silica polymorphs (quartz, chalcedony, and cristobalite). Hence, in the presence of excess aqueous Na and CO_2 (as is the case here), K-feldspar dissolution is the rate-limiting step for dawsonite precipitation, and aqueous silica concentrations quickly reach and maintain supersaturation with respect to all three silica polymorphs, which co-precipitate together with dawsonite.

Because K-feldspar dissolution is represented kinetically, in contrast to the equilibrium treatment of injection-induced aqueous CO_2 concentrations, initial dawsonite precipitation in model XSH is not coincident with initial plume ascent. Dawsonite cementation is first realized within the shale cap rock (basal 5 m layer only) at about 0.25 years; intra-plume dawsonite cementation begins at about 0.5 years. Once initiated, these processes continue throughout the prograde *and retrograde* regimes (Figure 8A-B). Reaction (2) proceeds to the right with an increase in solid-phase volume that varies from 17% (quartz and chalcedony) to 25.4% (cristobalite). However, K-feldspar comprises only 6.5% of the initial aquifer volume and reaction (2) has achieved only about 2.5% completion after 20 years; hence, aquifer porosity has been reduced by a factor of only 0.1% during this time, and would ultimately be reduced by a maximum factor of only 4%. As a result, for Sleipner-like settings the *coupled mineral dissolution/precipitation process* that results in dawsonite cementation has the desirable effect of maintaining initial CO_2 injectivity. The presence of intra-aquifer shales dramatically increases the spatial extent (but not concentration) of dawsonite cement in the near-field environment (Figure 8C-D).

Dawsonite cementation is unique among mineral-trapping mechanisms in that it is enabled by the composition of ambient formation waters—the high Na concentration of saline fluids (here, 0.45 molal). Hence, dawsonite cement is likely to form as a result of CO_2 injection into any saline aquifer that contains Al-bearing silicates (in particular, K-feldspar). In fact, natural analogs for this process have been documented: widespread dawsonite cement in the Bowen-Gunnedah-Sydney Basin, Eastern Australia, which has been interpreted to reflect magmatic CO_2 seepage on a continental scale (Baker et al., 1995), and sporadic dawsonite cement in the clastic Springerville-St. Johns CO_2 reservoir (Moore et al., 2003).

Plume-bounding precipitation of carbonate rind

Calcite-group carbonates (MCO_3) precipitate via distinct mechanisms along lateral and upper plume margins, effectively delineating the CO_2 storage volume. Both mechanisms can be described in the context of the following general precipitation reaction:

$$M^{+2} + CO_2(aq) + H_2O \leftrightarrow \underline{MCO_3} + 2\,H^{+}, \quad \text{for which} \qquad (3)$$

$$\log K = -(\log a_{M+2} + \log a_{CO2(aq)} + 2\,pH). \qquad (4)$$

Once the immiscible CO_2 plume has attained steady-state configuration, intra-plume $CO_2(aq)$ concentrations (which have increased, favoring MCO_3 precipitation) and pH (which has decreased, favoring MCO_3 dissolution) are maintained at nearly constant values. Given this

near-constant contribution of $-(\log a_{CO2(aq)} + 2\ pH)$ to log Q (the actual activity product) for reaction (4), typical saline-aquifer aqueous M^{+2} concentrations—such as those for Mg^{+2} and Ca^{+2} in this study—are insufficient to realize saturation with respect to any MCO_3.

However, these bulk ambient concentrations are continuously increased by silicate dissolution during the storage process. The rate of increase in intra-plume aqueous concentration for a specific M^{+2} depends on the abundance, M-concentration, and dissolution rate of M-bearing formation minerals; it also varies significantly with CO_2 saturation. Here, Mg^{+2} is available exclusively from phlogopite (2 solid-vol.%, 3 moles-Mg/mole-phlogopite), while Ca^{+2} is available exclusively from plag-Ab80 (5% solid-vol.%, 0.2 moles-Ca/mole-plag-Ab80). Hence, the source reservoir for Mg is roughly 6 times that of Ca. Moreover, the adopted specific surface area of phlogopite exceeds that of plag-Ab80 by a factor of almost 15, while its dissolution rate constant is only 30% smaller. As a result, in this model the bulk release rate for Mg from silicate dissolution will be roughly 60-70 times that of Ca. Because of this much larger release rate—and the larger background concentration of Mg (factor of 2.4, Table 3)—aqueous saturation with respect to magnesite is attained far more readily than that with respect to calcite, despite slightly higher solubility of the former.

While intra-plume aqueous M^{+2} concentrations are increasing during prograde disposal in model XSH, the aqueous flow direction is downward and slightly outward (Figure 3B). As the aqueous phase migrates across lateral plume boundaries along this path, H^+ concentration decreases by roughly 2.5 orders of magnitude (Figure 6B) while the corresponding decrease in CO_2(aq) concentration is only about half of that value (Figure 6E). This creates a background gradient in $-(\log a_{CO2(aq)} + 2\ pH)$ that is highly conducive to MCO_3 precipitation. Hence, lateral carbonate "rind" begins to precipitate along an outer shell (after about 0.25 years in model XSH), which marks the initial achievement of sufficient M^{+2} concentration. Then, as this concentration within migrating fluids continues to increase with time, this rind becomes more concentrated while growing upward and slightly inward from its outer shell, directly opposite to the flow direction. In model XSH, prograde magnesite rind forms by this process (Figure 9A), while sufficient Ca^{+2} concentrations to permit formation of coincident calcite rind are not achieved (Figure 9E).

During the retrograde regime, aqueous-phase flow directions are reversed. Hence, carbonate-undersaturated fluids are now migrating through prograde lateral rind along a gradient in $-(\log a_{CO2(aq)} + 2\ pH)$ that favors carbonate dissolution. However, along this traverse M^{+2} concentrations increase rapidly because of carbonate—and continued silicate—dissolution within outer portions of the prograde rind. As a result, the fluid quickly becomes saturated with respect to magnesite, which begins to precipitate just inside the outer shell and continues beyond this point. The net result is slow migration of the prograde lateral magnesite rind upwards and inward while its concentration increases (Figure 9B). This will continue as long as the Mg^{+2} source region is not exhausted. Continued plag-Ab80 dissolution during this time results in the initial development and subsequent growth of a retrograde lateral calcite rind (Figure 9F).

The influence of intra-aquifer shales on lateral rind formation is highly dependent on their lateral continuity. When such continuity exists (model CSH), the shales have little influence other than

vertical restriction of near-field rind development to beneath the lowest shale inter-bed (Figures 9C and 9G). In contrast, the presence of laterally discontinuous shales (model DSH) has two dramatic effects. First, spatially recursive lateral gradients in CO_2 aqueous solubility (Figure 7C-D) and pH (Figure 7G-H)—which develop around each column of focused vertical CO_2 migration (Figure 4C-D)—lead to similarly recursive precipitation of lateral carbonate rinds. During the prograde phase, they precipitate as "blooms" just above and to either side of each lateral break. During the retrograde regime, these blooms migrate away from the breaks, coalesce (from either side), and appear as mounds above each interior shale segment (Figure 9D). The second dramatic effect of lateral discontinuity is to create a highly irregular outer boundary to the residual saturation zone; this flattens the otherwise steep CO_2 aqueous solubility and pH gradients, leading to precipitation of much broader lateral rind (cf. Figures 9B,D). As a result of these two effects, the total mass of magnesite precipitated in lateral rind in model DSH is 75% greater than in models XSH and CSH.

Although a carbonate rind forms along *lateral* plume margins as a consequence of aqueous flow across steep gradients in pH and CO_2(aq) concentration, a similar rind also forms along *upper* plume boundaries in an environment of near-constant pH and CO_2(aq) concentration. Here, carbonate precipitation is enabled by its indirect dependence on CO_2 saturation. Specifically, for a given rate of M^{+2} hydrolysis from silicate dissolution the associated increase in *bulk* aqueous M^{+2} concentration is inversely proportional to thickness of the aqueous wetting fluid; i.e., proportional to CO_2 saturation. Hence, aqueous M^{+2} concentrations will increase far more rapidly within the prograde plume cap (where CO_2 saturation reaches 67%) than elsewhere, and may equilibrate with MCO_3 in the context of local pH and CO_2(aq) concentration. Moreover, because CO_2 saturation is maximized at the cap-rock interface, this is where MCO_3 cementation will initiate, and then expand downward into the aquifer. In model XSH, this process is exemplified by the formation of an upper magnesite rind, which begins to precipitate at the cap-rock interface after about 8 years, and then expands downward henceforth (Figure 9A-B). The identical process occurs in model CSH, where an upper magnesite rind develops beneath the cap rock and all intra-aquifer shales (Figure 9C), and in model DSH, where it develops only beneath the cap rock, but here to the greatest extent observed in the three models (Figure 9D). An upper calcite rind does not form owing to insufficient Ca^{+2} concentrations (Figures 9E-F).

Porosity evolution within the near-field environment reflects the integrated effect of the three distinct mineral dissolution/precipitation processes examined above. For Sleipner-like settings, this evolution is virtually negligible, although the individual contributions of intra-plume dawsonite cementation, lateral plume-bounding magnesite/calcite rind, and upper plume-bounding magnesite rind are readily distinguished (Figure 10). Hence, in these environments the *coupled mineral dissolution/precipitation process* that results in dawsonite cementation has the desirable effect of maintaining initial CO_2 injectivity, while those that form upper and lateral carbonate rind effectively delineate the CO_2 storage volume.

Carbonate cementation of intra-aquifer and cap-rock shales

The physical and compositional environment within which mineral trapping occurs in shales is distinct from that examined above for the saline aquifer. Chemical interaction of the immiscible

plume and shale mineralogy is primarily localized to shale interfaces with the underlying aquifer, but it also occurs along those intra-shale microfractures that permit some degree of immiscible CO_2 penetration. Here, the aqueous phase moves by advection and diffusion rates considerably slower that those characterizing the aquifer, while immiscible CO_2 interacts through this aqueous phase with a clay-dominated mineral assemblage whose bulk Fe-Mg concentration is much greater than that of the aquifer. This setting is far more conducive to Fe-Mg-carbonate cementation, because much larger aqueous Fe-Mg concentrations can be achieved through silicate dissolution.

In the present models, Fe-Mg-rich clays are represented by Mg-Chlorite, Fe-Mg carbonates are represented by magnesite, and the coupled mineral dissolution/precipitation reaction that leads to magnesite cementation can be expressed as:

$$\underset{\text{K-feldspar}}{\underline{KAlSi_3O_8}} + 2.5\ \underset{\text{Mg-chlorite}}{\underline{Mg_5Al_2Si_3O_{10}(OH)_8}} + 12.5\ CO_2(aq)$$

$$\leftrightarrow$$

$$\underset{\text{muscovite}}{\underline{KAl_3Si_3O_{10}(OH)_2}} + 1.5\ \underset{\text{kaolinite}}{\underline{Al_2Si_2O_5(OH)_4}} + 12.5\ \underset{\text{magnesite}}{\underline{MgCO_3}} + 4.5\ \underset{\text{qtz/chal}}{\underline{SiO_2}} + 6\ H_2O\ , \qquad (5)$$

whose stoichiometry follows from the relative magnitude among participating solids of both molar volumes and dissolution/precipitation volume fractions, the latter being predicted by the simulations.

Within the 25-m shale cap rock of models XSH, CSH, and DSH, magnesite precipitation is limited to the basal 10 m (represented by two 5-m layers of grid cells), where minimal immiscible CO_2 penetration occurs. Such precipitation is virtually limited to the basal 5-m layer, where near uniform magnesite concentration of 0.57 vol.% is obtained by the close of the prograde regime (Figure 11A); the analogous concentration in the overlying 5-m layer is 0.0023 vol.%. During the retrograde phase, immiscible CO_2 trapped beneath the cap rock continues to promote carbonate cementation in the basal 5-m layer, where near uniform magnesite concentration approaches 1.0 vol.% after 20 years (Figure 11B-D). This concentration is 20-30 times larger than those achieved within plume-bounding magnesite rinds (cf. Figures 9 and 11), reflecting the enhanced Mg concentrations and diminished aqueous flow rates within shale.

In models CSH and DSH, magnesite cementation of intra-aquifer shales is identical to that of the basal cap rock over the first 16-18 years. At this point, residual CO_2 saturation within these shales has been completely consumed through the aqueous phase by the cementation process (reaction 5), which therefore terminates. As a result, final magnesite concentrations within inter-bedded shales are slightly lower than in the basal cap rock (Figure 11C-D). Still, the presence of these shales causes the total mass of mineral-trapped CO_2 in models CSH and DSH to exceed that of model XSH by a factor of 3.0 and 1.8, respectively. However, even in model CSH composite mineral trapping accounts for only about 0.3% by mass of injected CO_2.

Although seemingly negligible, mineral trapping has enormous strategic significance because it continuously reduces shale porosity and permeability, and thereby continuously improves the isolation performance of shale cap rocks. This reduction process is exemplified by reaction (5), which proceeds to the right with a solid-phase volume increase of 18.5% (magnesite accounting for 47 vol.% of the product assemblage), and conveniently illustrated by porosity-permeability evolution within the basal cap rock of model XSH. Here, kinetic reaction (5) has attained roughly 15% completion after 20 years, reducing porosity by 8% (from 5 to 4.6%). Owing to adopted cubic dependence of the current-to-initial permeability ratio on that of porosity, this translates to a 22% reduction in permeability (Figure 12A).

Moreover, this reaction will proceed to completion unless the underlying immiscible CO_2 is completely exhausted, one of the reactant minerals is entirely consumed (or effectively armored by product phases against further dissolution), or shale porosity is fully sealed. Presuming the first two events do not occur, the third can be evaluated by extrapolating reaction (5) to hypothetical completion, which requires about 130 years. In this extreme case, final porosity of the basal cap-rock shale has been reduced by 52% from its original value, while permeability has been so reduced by 90%—an order of magnitude (Figure 12B). A natural analog to reaction (5) has recently been documented in the Ladbroke Grove natural gas field, where post-accumulation CO_2 influx has converted Fe-rich chlorite to Fe-rich dolomite (ankerite), kaolinite, and silica (Watson et al., 2002).

Screening criteria for identifying optimal storage sites in Sleipner-like settings

The simulation results examined above for models XSH, CSH, and DSH suggest preliminary screening criteria that can be used to identify optimal saline aquifer storage sites in Sleipner-like settings (shale-capped sandstone systems). These criteria fall into three fundamental groups: constraints on achieving optimal cap-rock performance and CO_2 injectivity, maximizing the spatial framework of plume-aquifer interaction, and enhancing efficacy of solubility and mineral trapping within this framework.

Optimal isolation performance ultimately hinges on the cap rock creating an effective hydrodynamic seal against vertical migration of the buoyant immiscible CO_2 plume. A 25-m-thick shale of typical porosity and permeability (5% and 3 μD, respectively: Freeze and Cherry, 1979) met this requirement in the simulations. However, trace immiscible CO_2 did penetrate this shale to 10 m during a relatively brief 10-year prograde regime; hence, this set of properties might be considered minimally effective—increased thickness and reduced permeability would be preferred. High concentrations of Fe-Mg-rich clays are also advantageous to maximize local carbonate cementation (e.g., reaction 5) and thereby continuously improve seal integrity. Lateral extent of the cap rock must be commensurate with the anticipated injection volume and topography of the aquifer/cap-rock interface. The underlying aquifer should be highly permeable, as in the simulations, to maximize CO_2 injectivity and minimize injection overpressures, which upon translation to the cap-rock interface in less permeable (or laterally

confined) systems may lead to geomechanical deformation of this seal (Johnson et al., 2003).

Given a secure cap rock and sufficient injectivity, the spatial framework of plume-aquifer interaction (i.e., CO_2 storage capacity) is maximized—and outward migration of the plume from the near-field environment delayed—by the presence of multiple inter-bedded lithologies that retard vertical and promote lateral plume migration, such as the thin shales in models CSH and DSH. By expanding the plume-formation water interface and source region for carbonate-forming cations, these inter-beds increase potential effectiveness of solubility and mineral trapping, the latter being still further enhanced if such units are laterally discontinuous (DSH).

Actual effectiveness of these trapping mechanisms is maximized by the presence of specific compositional constraints. Formation-water salinity should be moderate, as in the simulations; high enough to promote intra-plume dawsonite cementation, which roughly maintains initial CO_2 injectivity in the context of concomitant K-feldspar dissolution (reaction 2), but not so concentrated as to significantly reduce the effectiveness of solubility trapping (reaction 1). High concentrations of Fe-Mg-Ca-bearing minerals, uncharacteristic of the simulations, are required to maximize carbonate precipitation within upper and lateral plume-bounding rinds (reaction 3). Average elemental concentrations in unconsolidated sand aquifers (and in shales) are Fe > Mg > Ca (Blatt et al., 1972); for settings anomalously rich in Fe-Mg, the formation of such rinds may partially self-seal the plume. Ca concentrations are relatively small in both unconsolidated aquifers and shales (although the opposite is true for many carbonate-cemented sandstones); hence, in Sleipner-like settings, calcite is expected to play a minor role in mineral trapping relative to siderite, magnesite, and their solid solutions.

Concluding Remarks

Reactive transport modelling provides a unique methodology for identifying optimal geologic CO_2 storage sites and forecasting their long-term isolation performance. In the present contribution, we have used this approach to elucidate the fundamental processes, associated trapping mechanisms, and sequestration partitioning that will characterize saline-aquifer storage in Sleipner-like settings (shale-capped sandstone systems). Based on this analysis, we have proposed a preliminary set of physical and compositional constraints that portend optimal performance in these environments. Critical future investigations include quantifying sensitivity of predictive results—such as those reported here—to gaps and uncertainties in process models and parameters, quantifying sensitivity of isolation performance to site-specific variations in system characteristics, benchmarking key model predictions against well-constrained laboratory and large-scale field experiments, and extending the space-time framework to encompass far-field environments and millennia.

Extensive literatures document the gaps that exist within and uncertainty limits that surround many of the key process models and associated data adopted in this study. Particularly important are current gaps in the kinetic rate law for mineral precipitation (e.g., representation of various nucleation processes) and uncertainties in the relevant parameters (e.g., precipitation rate

constants, activation energies, supersaturation thresholds, and reactive specific surface areas). Accurate representation of multiphase flow processes hinges on uncertainties in several key parameters, such as residual gas and irreducible water saturations and the Van Genuchten sorting and bubble-pressure parameters, all of which are used to determine relative permeability and capillary pressure curves. Accurate representation of aqueous convection due to density instabilities that result from solubility trapping requires a rigorous equation of state for H_2O-NaCl-CO_2, which is approximated by that for H_2O in this study. Although we have made every effort to incorporate best-available process models and data in the simulations presented here, quantifying sensitivity of predictive results to the myriad uncertainties and approximations inherent to reactive transport modelling, such as those noted above, is critical for assigning to such results an appropriate level of confidence. Sensitivity analyses of this kind are also an effective means of prioritizing further refinement of key process models and parameters.

A number of potentially significant, but likely second-order, features and processes were not addressed in this study, and their presumed modifying influence on the fundamental processes and trapping mechanisms must be assessed. Particularly important to evaluate are the effects of intra-aquifer heterogeneity (i.e., viscous fingering), ambient flow, density-driven aqueous convection, and solid-solution compositions on the long-term stability and spatial distribution of solubility- and mineral-trapped CO_2, and the effect of aquifer-cap rock interface topography on the spatial distribution of hydrodynamically- and structurally-trapped CO_2. Explicit account of these effects—which can be accomplished with our current modelling capability—is required to assess their potential impact.

Identification of optimal saline-aquifer CO_2 storage sites requires quantifying sensitivity of isolation performance to the wide range of compositional, hydrological, structural, and depth variations that characterize these environments and proposed injection scenarios. Important compositional variations include those associated with waste-stream impurities (e.g., SO_x, NO_x, CH_4, H_2S), aquifer and cap-rock mineralogy (ranging from the presence of carbonate cements and silicate solid solutions in Sleipner-like settings to radically different lithologies such as anhydrite-capped carbonate systems), and the associated ambient aqueous phases (e.g., salinity and the concentrations of potential carbonate-forming cations). Important hydrological variations include CO_2 influx and ambient flow rates, aquifer and cap rock porosity and permeability (including their degree and style of heterogeneity), and residual gas and irreducible water saturations (Holtz, 2002, 2003). Important structural variations include lateral continuity, which together with CO_2 flux rate and aquifer permeability determine injection overpressures that translate to and may cause geomechanical deformation of the cap rock (Johnson et al., 2003), and topography of the aquifer-cap rock interface, which governs the up-dip migration path of underlying immiscible CO_2. Finally, system depth and the local geothermal gradient determine pressure-temperature conditions, which control phase relations within the equilibrium reference frame for mass transfer processes (e.g., solubility and mineral trapping) as well as the fluid-phase density contrasts that control buoyancy-driven immiscible CO_2 migration. Analyzing sensitivity of isolation performance to all of the above is an effective means of identifying key screening criteria, optimal storage sites, and determining the accuracy with which various system parameters need be measured.

Several of the predictive results from this study have important positive implications for the long-term efficacy of saline-aquifer CO_2 storage in Sleipner-like (and other) settings. These include the effect of residual CO_2 saturation to maintain or further enhance prograde trapping efficiency during the retrograde regime, and the effect of mineral trapping to maintain CO_2 injectivity (reaction 2), to delineate and partially self-seal the CO_2 storage volume (reaction 3), and to continuously improve the hydrodynamic seal integrity of shale cap rocks (reaction 5). This set of predictions can be assessed and refined through a series of integrated laboratory and modelling studies in which appropriately designed plug-flow and batch reactor experiments are conducted and simulated. They can also be benchmarked against relevant data obtained from field demonstrations, such as the US Frio project (Hovorka et al., 2002). Experimental and field corroboration of key predictive results is crucial because it represents the necessary point of departure for defensible extension of the reactive transport modelling approach to forecast the long-term isolation performance of commercial-scale saline aquifer CO_2 storage sites.

Acknowledgements

This work was performed under the auspices of the U.S. Department of Energy by the University of California, Lawrence Livermore National Laboratory under Contract W-7405-Eng-48. It is a pleasure to thank Etienne Brosse, Daniel Garcia, and Richard Worden for their thorough reviews of an earlier version of this manuscript; each contributed many insightful comments that were invaluable in preparing the revised contribution.

References

Baker, J.C., Bai, G.P., Hamilton, P.J., Golding, S.D., and Keene, J.B., 1995, Continental-scale magmatic carbon-dioxide seepage recorded by dawsonite in the Bowen-Gunnedah-Sydney Basin, Eastern Australia: J. Sed. Res., Sec. A – Sed. Petrol. Processes, v. 65, n. 3., p. 522-530.

Bertrand, C., Fritz, B., and Sureau, J.F., 1994, Hydrothermal experiments and thermo-kinetic modelling of water-sandstone interactions: Chem. Geol., v. 116, p. 189-192.

Berner, R.A., 1971, Principles of Chemical Sedimentology: McGraw-Hill, New York, 240 p.

Blatt, H., Middleton. G., and Murray, R., 1972, Origin of Sedimentary Rocks: Prentice-Hall, Englewood Cliffs, N.J., 634 p.

Blum, A.E., and Stillings, L.L., 1995, Feldspar dissolution kinetics: in White, A.F., and Brantley, S.L. (Eds.), Chemical Weathering Rates of Silicate Minerals: Rev. Min., v. 31, Min. Soc. Amer., Washington, DC, p 291-351.

Daveler, S.A., 1998, XTOOL 7.15 user's manual: Lawrence Livermore National Laboratory, UCRL-MA-130654, 32 p.

Drummond, S.E., 1981, Boiling and mixing of hydrothermal fluids: Chemical effects on mineral precipitation: unpub. Ph.D. diss., Pennsylvania State Univ.

Eiken, O., Brevik, I., Arts, R., Lindeberg, E., and Fagervik, K., 2000, Seismic monitoring of CO_2 injection into a marine aquifer: Proc. SEG Intl. Conf. 70th Ann. Mtg., 4 p.

Ennis-King, J., and Paterson, L., 2003, Role of convective mixing in the long-term storage of carbon dioxide in deep saline formations: Proc. SPE Ann. Tech. Conf., Denver, CO, October 5-8, 2003, 12 p.

Ennis-King, J., and Paterson, L., 2002, Rate of dissolution due to convective mixing in the underground storage of carbon dioxide: Proc. Sixth Intl. Conf. Greenhouse Gas Control Technologies (GHGT-6), Kyoto, Japan, Oct 1-4, 2002, v. 1, p. 507-510.

Fenghour, A., and Wakeman, W.A., 1998, The viscosity of carbon dioxide: J. Phys. Chem. Ref. Data, v. 27, n. 1, p. 31-44.

Fofonoff, P., and Millard, R.C., Jr., 1983, Algorithms for computation of fundamental properties of seawater: Unesco Technical Papers in Marine Sciences 44, 53 p.

Freeze, R.A., and Cherry, J.A., 1979, Groundwater: Prentice-Hall, Englewood Cliffs, NJ, 604 p.

Garrels, R.M., and Christ, C.L., 1965, Solutions, Minerals, and Equilibria: Freeman-Cooper, San Francisco, 450 p.

Gregersen, U., Johannessen, P.N., Møller, J.J., Kristensen, L., Christensen, N.P., Holloway, S., Chadwick, A., Kirby, G., Lindeberg, E., and Zweigel, P., 1998, Saline Aquifer CO_2 Storage S.A.C.S Phase Zero 1998. Internal report. GEUS (DK), BGS (UK), IKU (N). (provided courtesy of SACS)

Helgeson, H.C., 1969, Thermodynamics of hydrothermal systems at elevated temperatures and pressures: Amer. J. Sci., v. 267, p. 729-804.

Helgeson, H.C., Delany, J.M, Nesbitt, H.W., and Bird, D.K., 1978, Summary and critique of the thermodynamic properties of rock-forming minerals: Amer. J. Sci., v. 278-A, 229 p.

Holtz, M.H., 2003, Pore-scale influences on saline aquifer CO_2 sequestration: AAPG Annual Meeting, Salt Lake City, UT, May 11-14, 2003, v. 12, p. A79.

Holtz, M.H., 2002, Residual gas saturation to aquifer influx: A calculation method for 3-D computer reservoir model construction: Proc. SPE Gas Tech. Symp., Calgary, Alberta, Canada, April 30-May 2, 2002, 10 p.

Hovorka, S.D., Knox, P.R., Jackson, J.A, and Jackson, K.G., 2002, Frio brine sequestration pilot in the Texas gulf coast: Proc. Sixth Intl. Conf. Greenhouse Gas Control Technologies (GHGT-6), Kyoto, Japan, Oct 1-4, 2002, v. 1, p. 583-587.

Johnson, J.W., Knauss, K.G., Glassley, W.E., and DeLoach, L.D., and Tompson, A.F.B., 1998, Reactive transport modelling of plug-flow reactor experiments: quartz and tuff dissolution at 240^{o}C: J. Hydrol., v. 209, p. 81-111.

Johnson, J.W., and Lundeen, S.R., 1995, Facet: A graphical-user interface for viewing and updating the GEMBOCHS thermodynamic database: LLNL-YMP Milestone report MOL208, 28 p.

Johnson, J.W., and Lundeen, S.R., 1994a, Jewel: A graphical-user interface for generating custom GEMBOCHS thermodynamic datafiles for use with geochemical modelling software: LLNL-YMP Milestone report MOL63, 23 p.

Johnson, J.W., and Lundeen, S.R., 1994b, GEMBOCHS thermodynamic datafiles for use with the EQ3/6 software package: LLNL-YMP Milestone report MOL72, 99 p.

Johnson, J.W., and Nitao, J.J., 2002, Reactive transport modelling of geologic CO_2 sequestration at Sleipner: Proc. Sixth Intl. Conf. Greenhouse Gas Control Technologies (GHGT-6), Kyoto, Japan, Oct 1-4, 2002, v. 1, p. 327-332.

Johnson, J.W., Nitao, J.J., Morris, J.P., and Blair, S.C., 2003, Reactive transport modelling of geohazards associated with offshore CO_2 injection for EOR and geologic sequestration: Proc. Offshore Technology Conference, Houston, TX, May 5-8, 2003, 9 p.

Johnson, J.W., Nitao, J.J., Steefel, C.I., and Knauss, K.G., 2001, Reactive transport modelling of geologic CO_2 sequestration in saline aquifers: the influence of intra-aquifer shales and the relative effectiveness of structural, solubility, and mineral trapping during prograde and retrograde sequestration: Proc. First Natl. Conf. Carbon Seqn., Washington, DC, May 14-17, 2001, 60 p. [UCRL-JC-146932]

Johnson, J.W., Nitao, J.J., Tompson, A.F.B., Steefel, C.I., *et al*., 1999, 21st-century tools for modelling reactive transport in dynamic geologic systems of economic and environmental significance: in Earth and Environmental Sciences 1998 Annual Report, p. 7-11, LLNL, UCRL-LR-126434-98.

Johnson, J.W., and Norton, D., 1991, Critical phenomena in hydrothermal systems: State, thermodynamic, electrostatic, and transport properties of H_2O in the critical region: Amer. J. Sci., v. 291, pp. 541-648.

Johnson, J.W., Oelkers, E.H., and Helgeson, H.C., 1992, SUPCRT92: A software package for calculating the standard molal thermodynamic properties of minerals, gases, aqueous species, and reactions from 1 to 5000 bars and 0 to 1000C: Computers and Geosciences, v. 18, n. 7, p. 899-947.

Jordan, G., and Rammensee, W., 1998, Dissolution rates of calcite (1014) obtained by scanning force microscopy: Microtopography-based dissolution kinetics on surfaces with anisotropic step velocities: Geochim. Cosmochim. Acta, v. 62, n. 6., p. 941-947.

Knauss, K.G., and Copenhaver, S.A., 1995, The effect of malonate on the dissolution kinetics of albite, quartz and microcline as a function of pH at 70^{o}C: Applied Geochem., v. 10, n. 1, p. 17-33.

Knauss, K.G., and Wolery, T.J., 1989, muscovite dissolution kinetics as a function of pH and time at 70^{o}C: Geochim. Cosmochim. Acta, v. 53, p. 1493-1501.

Knauss, K.G., and Wolery, T.J., 1988, The dissolution kinetics of quartz as a function of pH and time at 70^{o}C: Geochim. Cosmochim. Acta, v. 52, p. 43-53.

Knauss, K.G., and Wolery, T.J., 1986, Dependence of albite dissolution kinetics on pH and time at 25^{o}C and 70^{o}C: Geochim. Cosmochim. Acta, v. 50, p. 2481-2497.

Lasaga, A.C., 1998, Kinetic Theory in the Earth Sciences: Princeton Univ. Press, Princeton, NJ, 811 p.

Lindeberg, E., and Bergmo, P., 2002, The long-term fate of CO_2 injected into an aquifer: Proc. Sixth Intl. Conf. Greenhouse Gas Control Technologies (GHGT-6), Kyoto, Japan, Oct 1-4, 2002, v. 1, p. 489-494.

Meyer, C.A., McClintock, R.B, and Silvestri, G.J., 1993, ASME Steam Tables: Thermodynamic and Transport Properties of Steam (comprising tables and charts for steam and water, calculated using the 1967 IFC formulation for industrial use, in conformity with the 1963 international skeleton tables, as adopted by the Sixth International Conference on the Properties of Steam), 6^{th} ed., ASME, New York, 436 p.

Moore, J., Adams, M., Allis, R., Lutz, S., and Rauzi, S., 2003, Investigations of CO_2 mobility in natural reservoirs beneath the Colorado Plateau and Southern Rocky Mountains, Proc. Second Annual Conference on Carbon Sequestration, May 5-8, 2003, Alexandria, Virginia, 22 p.

Nagy, K.L., 1995, Dissolution and precipitation kinetics of sheet silicates: in White, A.F., and Brantley, S.L. (Eds.), Chemical Weathering Rates of Silicate Minerals: Rev. Min., v. 31, Min. Soc. Amer., Washington, DC, p 173-233.

Nitao, J.J., 1998a, Reference manual for the NUFT flow and transport code, version 2.0: Lawrence Livermore National Laboratory, UCRL-MA-130651, 55 p.

Nitao, J.J., 1998b, User's manual for the USNT module of the NUFT Code, Version 2.0 (NP-Phase, NC-component, Thermal): Lawrence Livermore National Laboratory, UCRL-MA-130653, 76 p.

Norton, D., 1984, Theory of hydrothermal systems: Ann. Rev. Earth Planet. Sci., v. 12, p. 155-177.

Parker, J.C., Lenhard, R.J., and Kuppusamy, T., 1987, A parametric model for constitutive properties governing multiphase flow in porous media: Water Resources Research, v. 23, n. 4, p. 618-624.

Pokrovsky, O.S., and Schott, J., 1999, Processes at the magnesium-bearing carbonates solution interface. II. Kinetics and mechanism of magnesite dissolution: Geochim. Cosmochim. Acta, v. 63, n. 6, p. 881-897.

Renders, P.J.N., Gammons, C.H., and Barnes, H.L., 1995, Precipitation and dissolution rate constants for cristobalite from 150 to 300^{o}C: Geochim. Cosmochim. Acta, v. 59, n. 1, p. 77-85.

Robie, R.A., Hemingway, B.S., and Fisher, J.R., 1978, Thermodynamic properties of minerals and related substances at 298.15 K and 1 bar (10^5 Pascals) pressure and at higher

temperatures: U.S.G.S. Bull. 1452, 456 p.

SACS, 2000, Final Technical Report "SACS" – Saline Aquifer CO_2 Storage, 34 p. (available on the SACS web site: http://www.ieagreen.org.uk/sacshome.htm)

Scheidegger, A.E., 1974, The Physics of Flow through Porous Media (3rd ed.): Univ. Toronto Press, Toronto, 353 p.

Shock, E.L., 1998, An updated and augmented version (slop98.dat) of the original SUPCRT92 database (sprons92.dat) is available on the Dr. Shock's website: http://zonvark.wustl.edu/geopig/

Shock, E.L., Oelkers, E.H., Johnson, J.W., Sverjensky, D.A., and Helgeson, H.C., 1992, Calculation of the thermodynamic properties of aqueous species at high pressures and temperatures: Effective electrostatic radii, dissociation constants, and standard partial molal properties to 1000C and 5 kb: Journal of the Chemical Society (London) Faraday Transactions, v. 88, n. 6, p. 803-826.

Span, R., and Wagner, W., 1996, A new equation of state for carbon dioxide covering the fluid region from the triple-point temperature to 1100 K at pressures up to 800 MPa: J. Phys. Chem. Ref. Data, v. 25, n. 6, p. 1509-1596.

Stillings, L.L., Drever, J.I., Brantley, R.L., Sun, Y., and Oxburgh, R., 1996, Rates of feldspar dissolution at pH 3-7 with 0-8 mM oxalic acid: Chem. Geol., v. 132, p. 79-89.

Tanger, J.C. IV, and Helgeson, H.C., 1988, Calculation of the thermodynamic and transport properties of aqueous species at high pressures and temperatures: Revised equations of state for the standard partial molal properties of ions and electrolytes: Amer. J. Sci., v. 288, n. 1, p. 19-98.

Tester, J.W., Worley, W.G., Robinson, B.A., Grigsby, C.O., and Feerer, J.R., 1994, Correlating quartz dissolution rates in pure water from 25 to 625°C: Geochim. Cosmochim. Acta, v. 58, n. 11, p. 2407-2420.

Watson, M.N., Zwingmann, N., and Lemon, N.M., 2002, The Ladbroke Grove-Katnook carbon dioxide natural laboratory: A recent CO_2 accumulation in a lithic sandstone reservoir, Proc. Sixth Intl. Conf. Greenhouse Gas Control Technologies (GHGT-6), Kyoto, Japan, Oct 1-4, 2002, p. 435-440.

Table 1: Pressure-temperature conditions, porosities, and permeabilities reported for the saline aquifer, shale cap rock, and intra-aquifer shales at Sleipner and those adopted in this study.

parameter	**Utsira Formation**[a]	**saline aquifer**[b]	**shale cap rock**[b,c]	**intra-aquifer shales (CSH)**[b,c]	**intra-aquifer shales (DSH)**[b,c]
T (^{o}C)	37	37	37	37	37
P (bars)	80-110	90-110	87.5-90	---	---
poros. (%)	35-40	35	5[d]	5[d]	5[d]
perm. (m^2)	(1-8)(10^{-12})	3(10^{-12})	3(10^{-18})[d]	3(10^{-15})[e]	3(10^{-18})[d]
thickness (m)	150-250	200	25	3	3

[a] Gregersen et al. (1998)
[b] adopted in this study
[c] data from or directly representative of Sleipner are unavailable
[d] average values (Freeze and Cherry, 1979)
[e] modified from average value (Freeze and Cherry, 1979) per adopted density and aperture of microfractures; see text

Table 2: Saline-aquifer and shale mineralogies reported at Sleipner and those adopted in this study; abundances are given in volume percent.

mineral	**Miocene sand**[a]	**saline aquifer**[b]	**shale**[b,c]
quartz	79	80[f]	35
K-feldspar	6	10[f]	5
Plagioclase	3	5[f]	0
"Mica"	5[d]	0	0
calcite	5[e]	0	0
"Clay"	1	0	0
muscovite	0	3	50[h]
phlogopite[i]	0	2	0
Mg-chlorite[i,j]	0	0	10[h]
grain diameter[k] (mm)	unreported	0.25[l]	0.025[m]

[a] provided by Tore Torp (Statoil) and Niels Springer (GEUS) as a proxy for an analysis from the Utsira Formation (pers. comm.)

[b] adopted in this study

[c] data from or directly representative of Sleipner are unavailable; adopted mineralogy (60% clay minerals, 35% quartz, 5% feldspar) is based on average shale compositions (Blatt et al., 1972)

[d] incorporated as 3% muscovite and 2% phlogopite, the latter as a proxy for trace glauconite and biotite, which have been reported for the Utsira (Gregersen et al., 1998)

[e] eliminated per unconsolidated nature of the Utsira, which implies a lack of carbonate cement

[f] augmented per elimination of calcite (see previous footnote)

[h] representing the 60% clay fraction with this muscovite/Mg-chlorite ratio preserves the typical $K_2O/(MgO+FeO)$ ratio of shales (Blatt et al., 1972), while permitting avoidance of more realistic illite, smectite, and montmorillonite solid solutions, for which thermodynamic and kinetic data are lacking

[i] Mg end-member component used to represent Fe-Mg solid solutions (see text)

[j] clinochlore-14A

[k] nominal value based on the Udden-Wentworth size grade scale

[l] consistent with "fine to medium grained sand", which has been reported for the Utsira formation (SACS, 2000)

[m] consistent with "mixture of very fine sand, silt, and clay particles", which typifies shale lithologies (Blatt et al., 1972)

Table 3: Aqueous concentrations (in molality) reported for seawater, the Utsira formation at Oseberg, and those adopted in this study

component	seawater[a]	Oseberg[b]	this study[c]
Sodium	0.48	0.4520	Oseberg
Potassium	0.010	0.0053	Oseberg
Calcium	0.010	0.0106	0.00742[d]
Magnesium	0.054	0.0259	0.01813[d]
Strontium	unreported	$1.14(10^{-4})$	0[e]
Barium	unreported	$3.64(10^{-6})$	0[e]
Aluminum	unreported	unreported	$1.3(10^{-8})$[f]
Silica	unreported	unreported	$1.664(10^{-4})$[g]
Iron [total]	unreported	$3.58(10^{-5})$	0[h]
Chloride	0.56	0.5213	Oseberg
Bicarbonate	0.0024	0.0116	0.00232[i]
Carbonate	$2.7(10^{-4})$	unreported	---[j]
Sulphate	0.028	undetected	Oseberg (0)
Oxygen [O_2(aq)] (ppb)	unreported	5	0[k]
pH	8.15	7.1	7.0-7.2[l]

[a] average surface seawater at 25°C (Garrels and Christ, 1965)
[b] from Gregersen et al. (1998), who report concentrations in g/L; this analysis is from the Utsira at Oseberg, about 200 km north of Sleipner
[c] adopted for both the saline aquifer and shale units
[d] 70% of Oseberg value; reduced to obtain undersaturation with respect to calcite and magnesite per the absence of carbonate cement in the Utsira
[e] trace concentrations removed
[f] between K-feld+Mucovite and kaolinite+quartz equilibrium (37°C, 100 bars)
[g] quartz equilibrium (37°C, 100 bars)
[h] removed because ferrous/ferric partitioning cannot be constrained (see footnote k)
[i] 20% of Oseberg value (roughly equivalent to average seawater); reduced to obtain undersaturation with respect to calcite and magnesite per the absence of carbonate cement in the Utsira; ambient bicarbonate concentration (reduced or not) is completely overwhelmed by the effect of CO_2 injection
[j] in this study, "bicarbonate" concentration combines both bicarbonate and carbonate contributions
[k] removed because the Oseberg value cannot represent an *in situ* concentration; at 37°C, 110 bars, it defines an equilibrated O_2(g) fugacity of $10^{-3.8}$ (cf. the magnetite-hematite buffer under these conditions: $10^{-69.0}$); hence, the reported O_2(aq) cannot be used to constrain the ambient oxidation state and dependent ferrous/ferric partitioning
[l] range encompasses extra-plume pH evolution within both the saline aquifer and all shales over the 20-year simulation

Table 4: Adopted kinetic data for primary (boldface) and observed (precipitated) secondary minerals

mineral	P_r-T_r diss/pptn rate constant[a,b] (mol m^{-2} s^{-1})	activation energy[a] (kJ mol^{-1})	reactive specific surface area[c] (m^2 m^{-3})$_{mineral}$	surface area scaling factor[d]
quartz	$1.035(10^{-14})$[e]	87.7[e]	$5.741(10^4)$	2.39
K-feldspar	$1.778(10^{-10})$[f]	51.7[f]	$1.113(10^5)$	4.64
plag-Ab80	$5.623(10^{-13})$[f]	80.3[f]	$8.752(10^4)$	3.65[iq]
muscovite	$1.000(10^{-13})$[g]	22.0[g]	$1.246(10^6)$	51.90
phlogopite	$4.000(10^{-13})$[g]	29.0[g]	$1.246(10^6)$	51.90[n]
Mg-chlorite[p]	$3.000(10^{-13})$[g]	88.0[g]	$1.246(10^6)$	51.90[n]
magnesite	$1.000(10^{-9})$[h]	62.8[i]	---	---
dawsonite	$1.000(10^{-7})$[il]	62.8[i]	---	---
calcite	$1.500(10^{-6})$[j]	62.8[i]	---	---
cristobalite	$3.450(10^{-13})$[k]	62.8[i]	---	---
chalcedony	$3.450(10^{-13})$[im]	62.8[i]	---	---
kaolinite	$4.000(10^{-13})$[g]	29.0[g]	---	---
talc	$1.000(10^{-12})$[g]	42.0[g]	---	---
paragonite	$1.000(10^{-13})$[in]	22.0[in]	---	---
pyrophyllite	$4.000(10^{-13})$[io]	29.0[io]	---	---
gibbsite	$3.000(10^{-13})$[g]	62.8[i]	---	---

[a] adopted data are those for the relevant acidic conditions (pH 4-5.5), which characterize the intra-plume aqueous phase during both prograde and retrograde regimes

[b] dissolution and precipitation rate constants are taken to be of equal magnitude, recognizing that this approximation is crude in some cases

[c] specific surface areas (SSA) are those of representative spheres (see Table 2) multiplied by the surface area scaling factor; *reactive* SSA are SSA multiplied by the fraction of SSA presumed in contact with the aqueous phase; reactive SSA for each mineral is equivalent in the aquifer and shales (see text)

[d] factor of increase observed for 100-μm grains whose SSA has been measured using BET methods by Knauss and Copenhaver (1995), Knauss and Wolery (1989, 1988, 1986), and Stillings et al. (1996)

[e] Tester et al. (1994); [f] Blum and Stillings (1995); [g] Nagy (1995)

[h] Pokrovsky and Schott (1999); [i] estimated in the present study

[j] Jordan and Rammensee (1998); [k] Renders et al. (1995)

[l] estimated as intermediate to calcite and magnesite

[m] presumed equivalent to cristobalite

[n] presumed equivalent to muscovite

[o] presumed equivalent to kaolinite

[p] clinochlore-14A

[q] based on observed scaling factors for albite and anorthite

Figure Captions

Figure 1. Schematic depiction of interdependent subsurface processes that redistribute mass and energy in response to the disequilibrium state (lateral T, P, ρ_f gradients) imposed by natural or engineered perturbation events. Porosity and permeability are the key variables that link thermal-hydrological (blue), geomechanical (maroon), and geochemical (aqua) sectors of the diagram.

Figure 2. Schematic depiction of (A) CO_2 injection into a saline aquifer at Statoil's North Sea Sleipner facility and (B-D) the spatial domains adopted for reactive transport simulation of the near-field environment (region within a few 100 m of the injection well) in models XSH, CSH, and DSH.

Figure 3. CO_2 immiscible saturation in model XSH. (A) Prograde residual saturation tracks initial ascent of the plume, whose steady-state configuration obtains within one year; (B) cap-zone saturation slowly increases during prograde migration; (B-C) injection-induced aqueous flow reverses direction at the prograde/retrograde transition; (D) residual saturation drives retrograde trapping mechanisms.

Figure 4. CO_2 immiscible saturation during prograde and retrograde plume migration for models CSH and DSH. Spatial extent of the steady-state plume for CSH and DSH exceeds that of XSH by factors of 3.2 and 1.4, respectively.

Figure 5. Plume configuration after 3 years in models XSH, CSH, and DSH as compared to that observed seismically at Sleipner, which strongly suggests that the Utsira combines elements of models CSH and DSH.

Figure 6. CO_2 aqueous concentrations (composite molality of all carbon-bearing aqueous solutes) and pH in model XSH during prograde (1 and 10 years) and retrograde (20 years) regimes.

Figure 7. CO_2 aqueous concentrations (composite molality of all carbon-bearing aqueous solutes) and pH in models CSH and DSH at the close of prograde (10 years) and retrograde trapping (10 years).

Figure 8. Intra-plume dawsonite cementation at the close of (A) prograde mineral trapping for model XSH and (B-D) retrograde trapping for models XSH, CSH, and DSH.

Figure 9. Magnesite and calcite components of carbonate rind that delineates lateral and upper plume boundaries at the close of (A-B) prograde mineral trapping for model XSH and (C-H) retrograde trapping for models XSH, CSH, and DSH. Intra-aquifer and basal cap-rock shales have magnesite >0.05 vol.% (white regions) and calcite typically <0.005 vol.% (trace concentrations in G-H).

Figure 10. Saline aquifer porosity at the close of (A) prograde mineral trapping for model XSH and (B-D) retrograde trapping for models XSH, CSH, and DSH.

Figure 11. Magnesite precipitation within basal cap-rock and intra-aquifer shales at the close of (A) prograde mineral trapping for model XSH and (B-D) retrograde trapping for models XSH, CSH, and DSH. The 20-30 fold increase in magnesite concentration from plume-bounding rind (Fig. 9) to shale primarily reflects that of initial bulk Mg.

Figure 12. Interdependent porosity-permeability evolution due to kinetic progression of reaction (5) within the basal shale cap rock of model XSH (A) at the close of the retrograde phase, and (B) as extrapolated to completion, which requires 130 years.

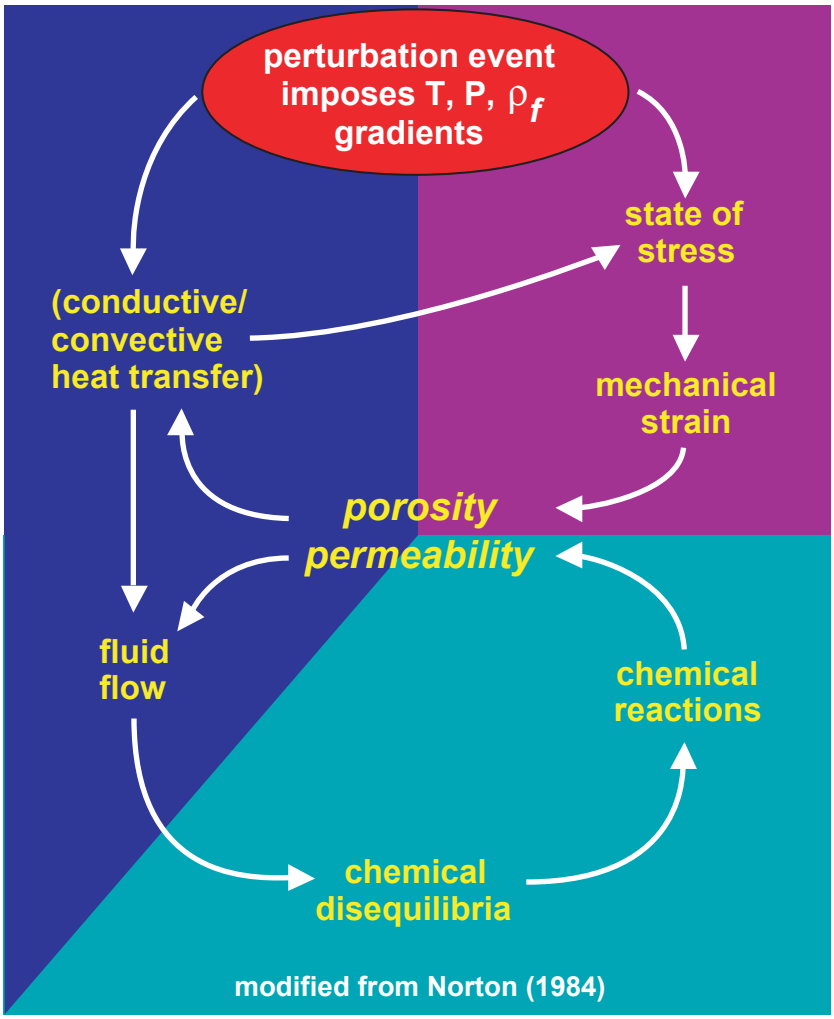
perturbation event
imposes T, P, ρ_f
gradients
state of
stress
(conductive/
convective
heat transfer)
mechanical
strain
porosity
permeability
fluid
flow
chemical
reactions
chemical
disequilibria
modified from Norton (1984)

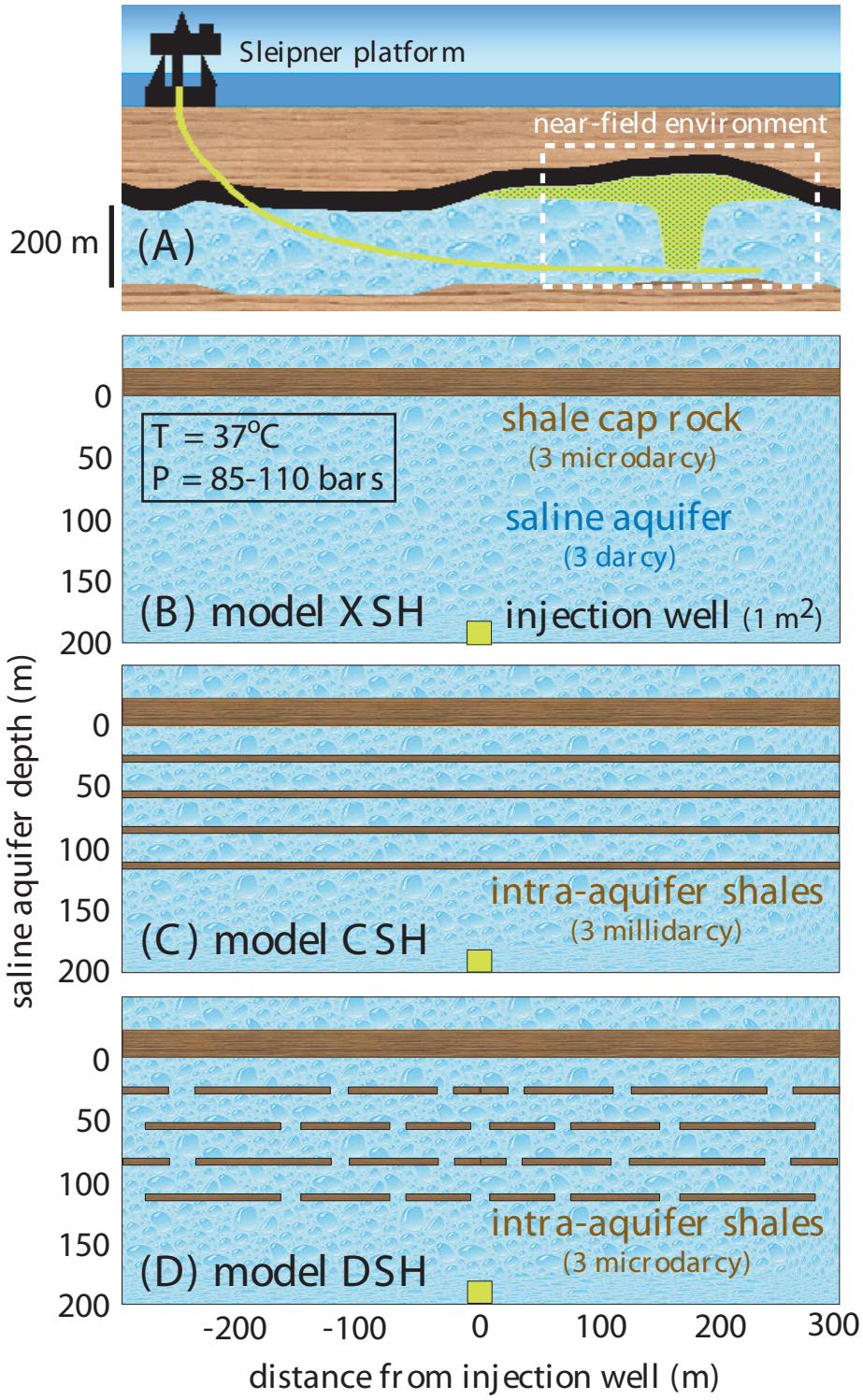
Sleipner platform
near-field environment
200 m
(A)
T = 37°C
P = 85-110 bars
shale cap rock
(3 microdarcy)
saline aquifer
(3 darcy)
(B) model XSH
injection well (1 m2)
(C) model CSH
intra-aquifer shales
(3 millidarcy)
(D) model DSH
intra-aquifer shales
(3 microdarcy)
saline aquifer depth (m)
0
50
100
150
200
-200
-100
0
100
200
300
distance from injection well (m)

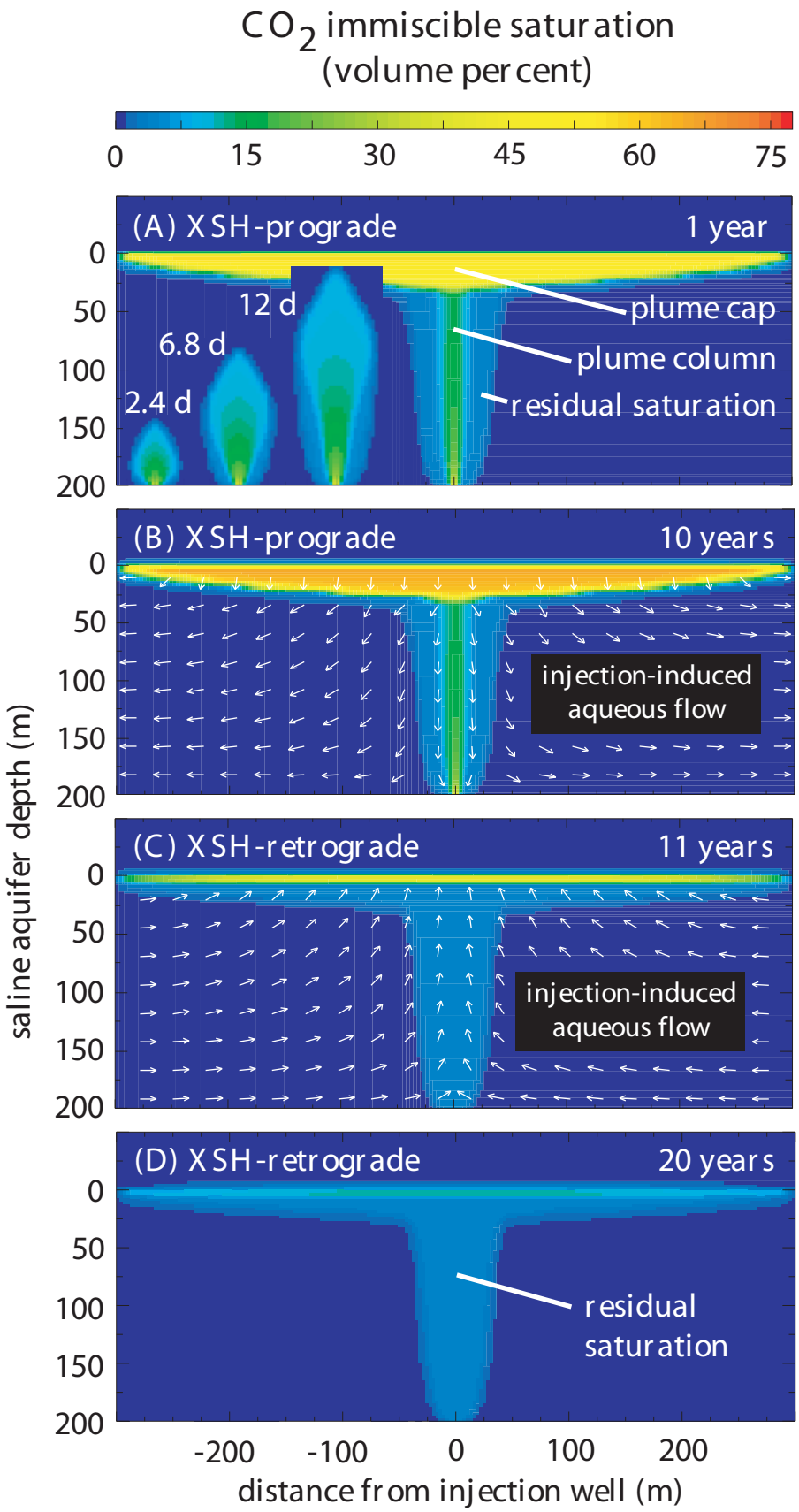
CO2 immiscible saturation
(volume percent)
0
15
30
45
60
75
(A) XSH-prograde
1 year
12 d
6.8 d
2.4 d
plume cap
plume column
residual saturation
(B) XSH-prograde
10 years
injection-induced
aqueous flow
(C) XSH-retrograde
11 years
injection-induced
aqueous flow
(D) XSH-retrograde
20 years
residual
saturation
saline aquifer depth (m)
0
50
100
150
200
-200
-100
0
100
200
distance from injection well (m)

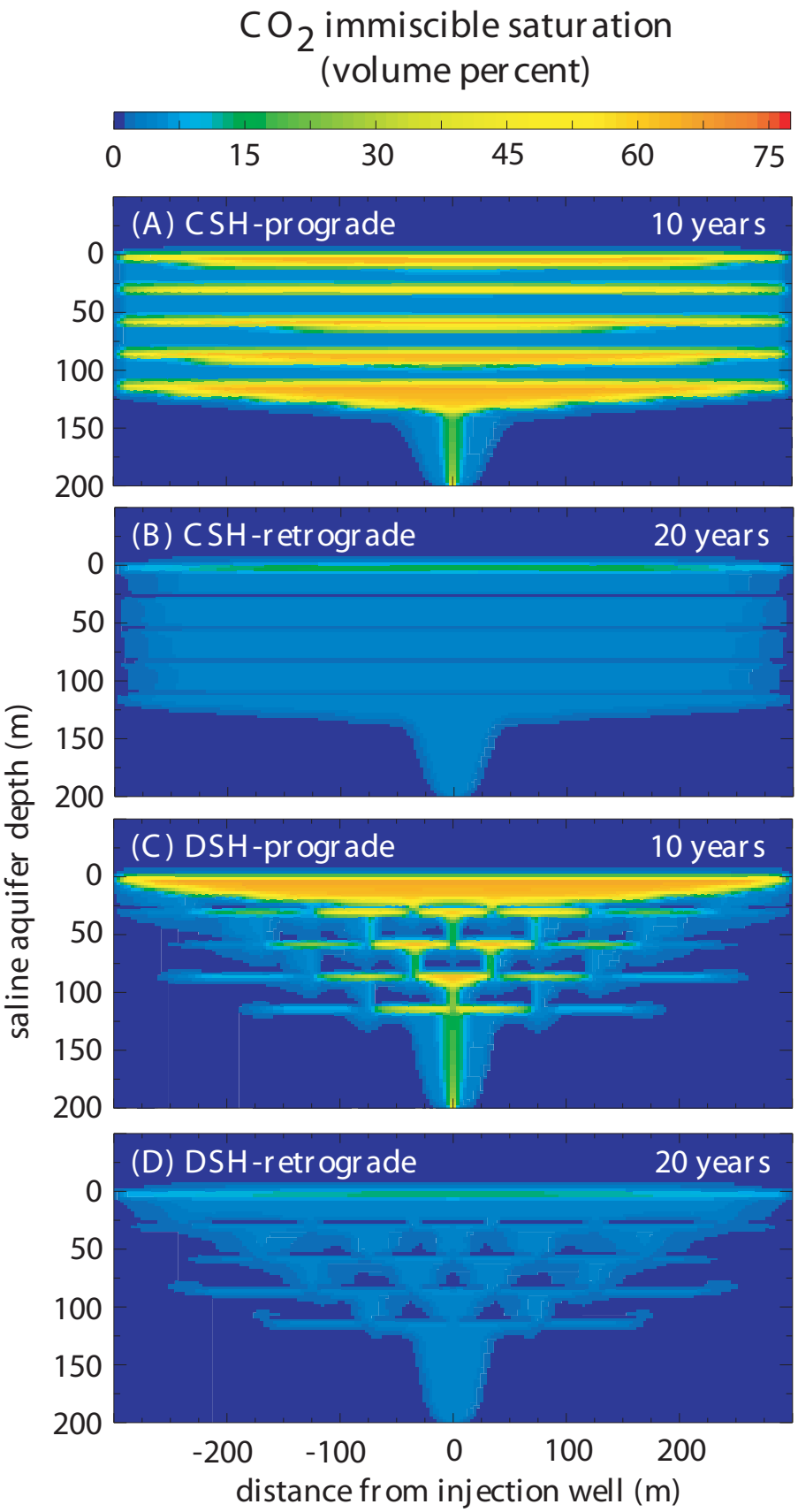
CO2 immiscible saturation
(volume percent)
0
15
30
45
60
75
(A) CSH-prograde
10 years
(B) CSH-retrograde
20 years
(C) DSH-prograde
10 years
(D) DSH-retrograde
20 years
saline aquifer depth (m)
0
50
100
150
200
-200
-100
0
100
200
distance from injection well (m)

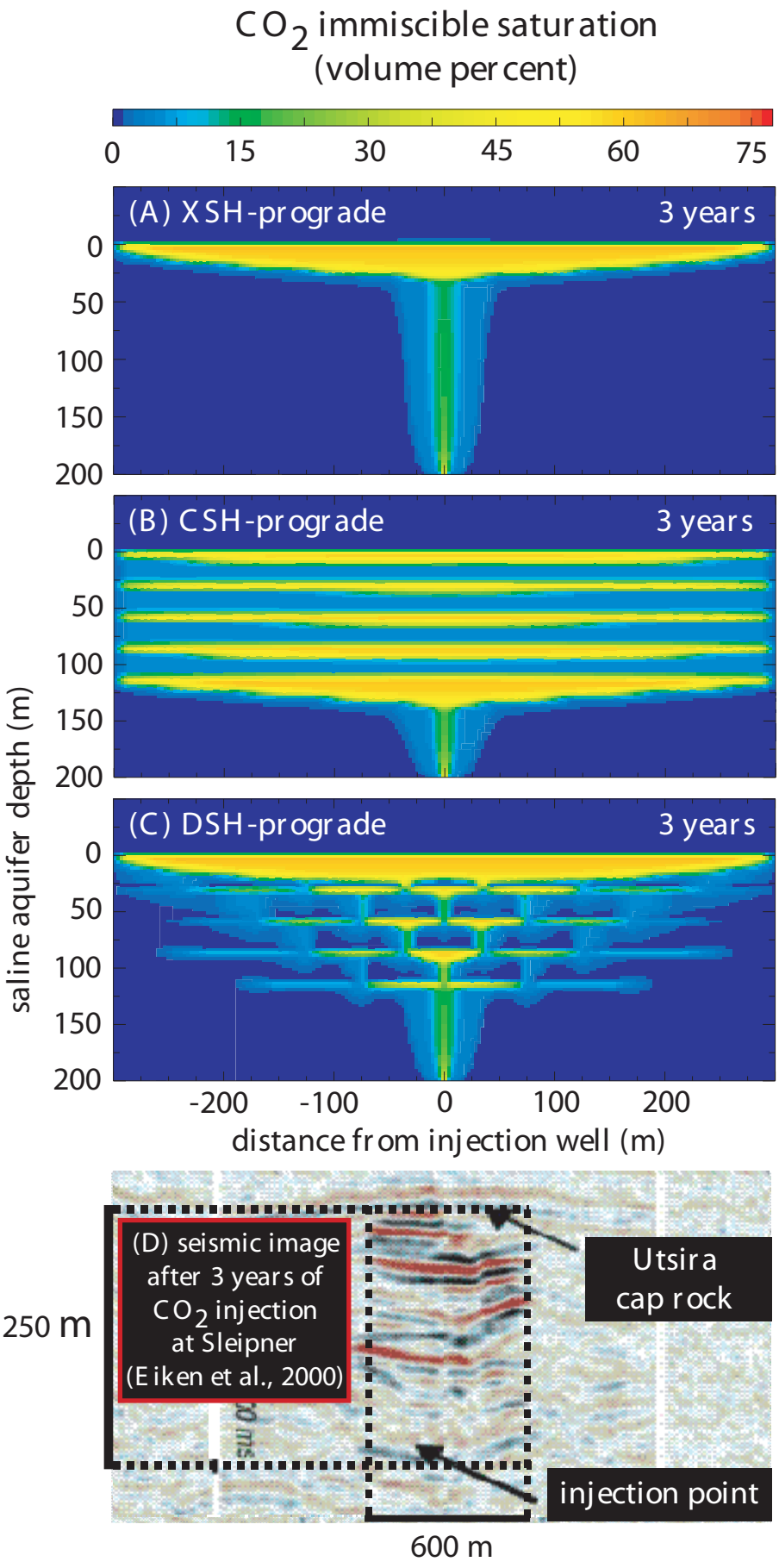
CO2 immiscible saturation
(volume percent)
0
15
30
45
60
75
(A) XSH-prograde
3 years
(B) CSH-prograde
3 years
(C) DSH-prograde
3 years
0
50
100
150
200
saline aquifer depth (m)
-200
-100
0
100
200
distance from injection well (m)
(D) seismic image after 3 years of CO2 injection at Sleipner (Eiken et al., 2000)
Utsira cap rock
injection point
250 m
600 m

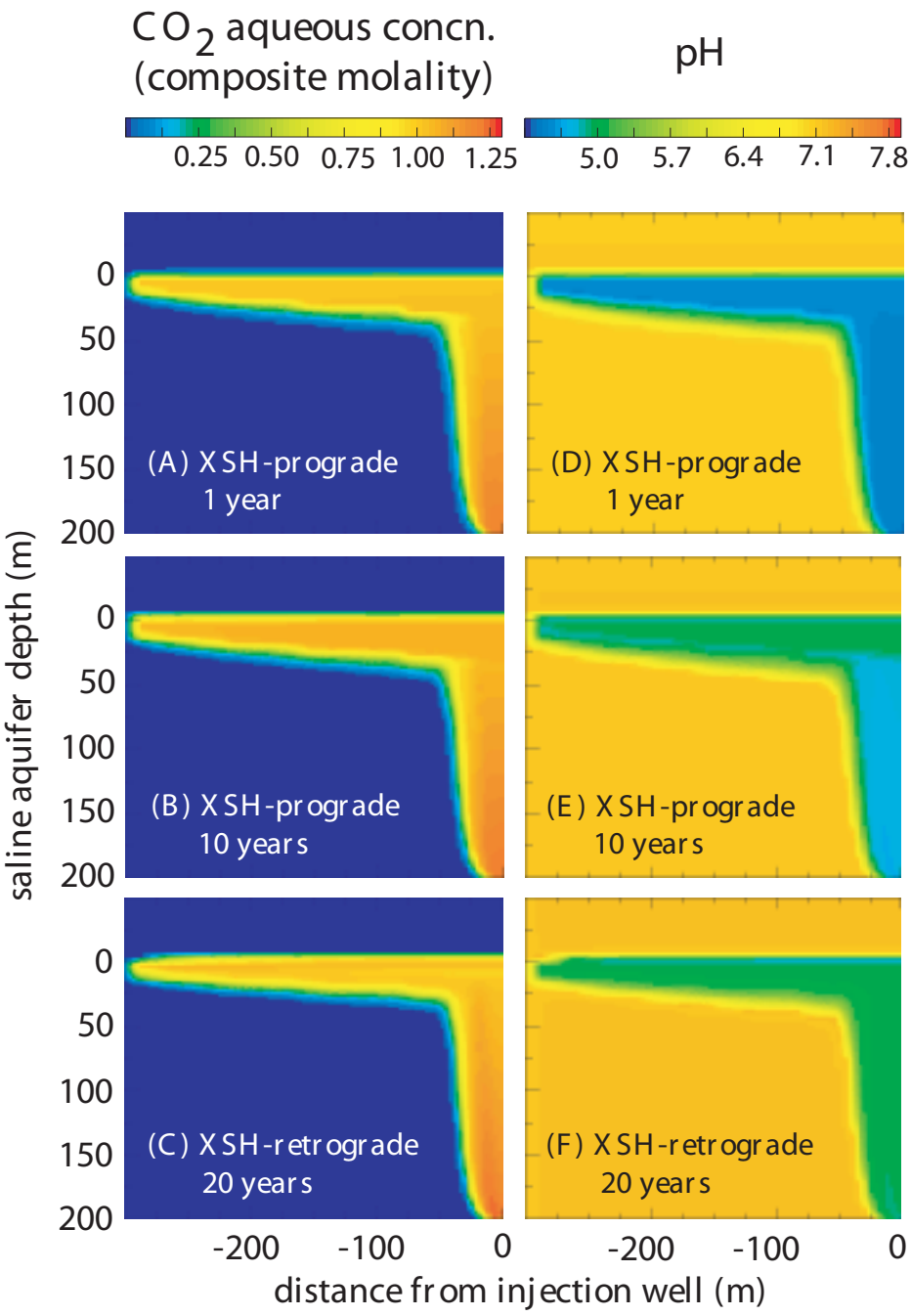
CO2 aqueous concn.
(composite molality)
0.25 0.50 0.75 1.00 1.25
pH
5.0 5.7 6.4 7.1 7.8
(A) XSH-prograde
1 year
(D) XSH-prograde
1 year
(B) XSH-prograde
10 years
(E) XSH-prograde
10 years
(C) XSH-retrograde
20 years
(F) XSH-retrograde
20 years
saline aquifer depth (m)
0
50
100
150
200
-200
-100
0
distance from injection well (m)

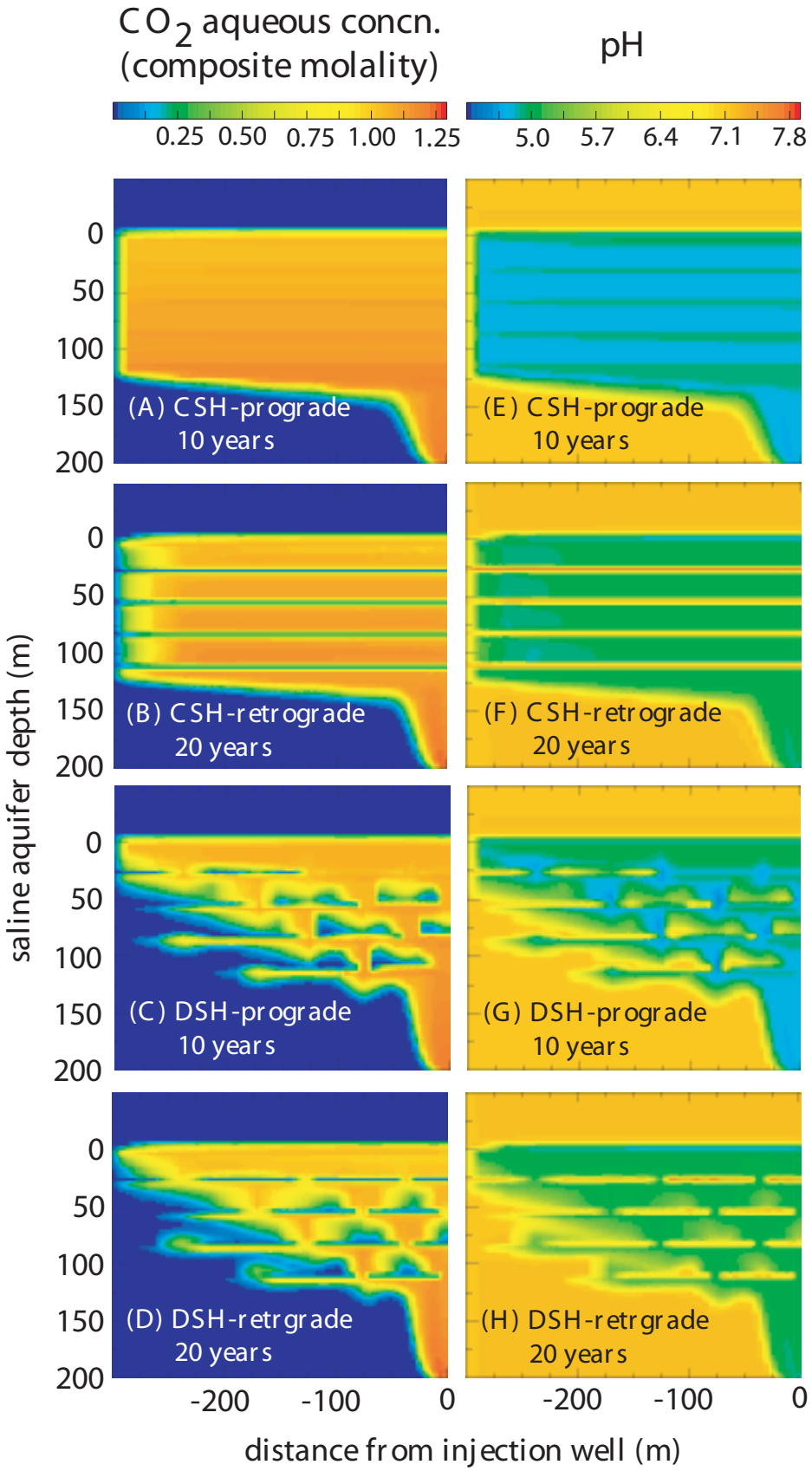
CO2 aqueous concn. (composite molality)
0.25 0.50 0.75 1.00 1.25
pH
5.0 5.7 6.4 7.1 7.8
saline aquifer depth (m)
0
50
100
150
200
(A) CSH-prograde 10 years
(E) CSH-prograde 10 years
(B) CSH-retrograde 20 years
(F) CSH-retrograde 20 years
(C) DSH-prograde 10 years
(G) DSH-prograde 10 years
(D) DSH-retrgrade 20 years
(H) DSH-retrgrade 20 years
-200 -100 0
distance from injection well (m)

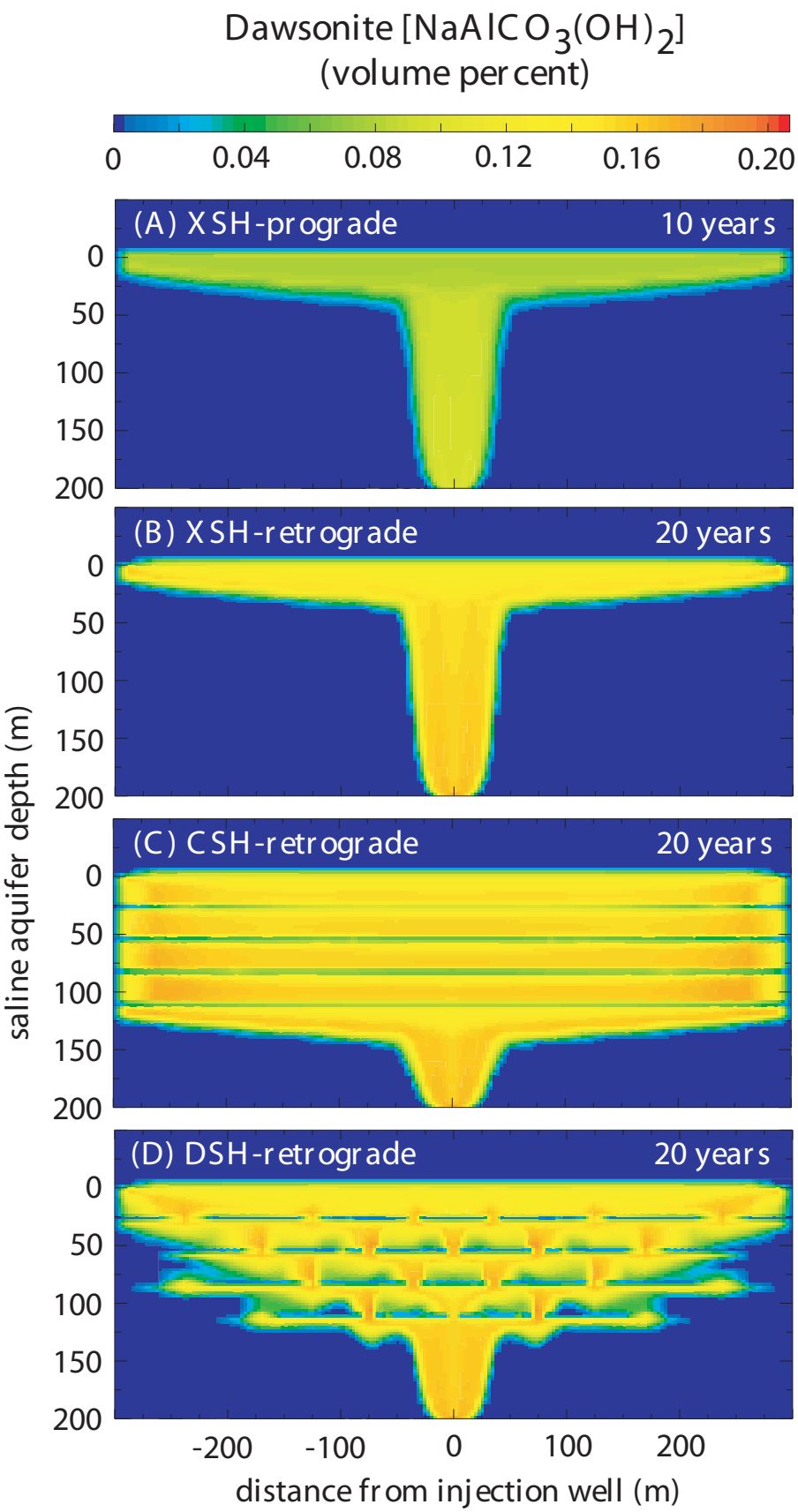
Dawsonite [NaAlCO3(OH)2]
(volume percent)
0
0.04
0.08
0.12
0.16
0.20
(A) XSH-prograde
10 years
(B) XSH-retrograde
20 years
(C) CSH-retrograde
20 years
(D) DSH-retrograde
20 years
0
50
100
150
200
saline aquifer depth (m)
-200
-100
0
100
200
distance from injection well (m)

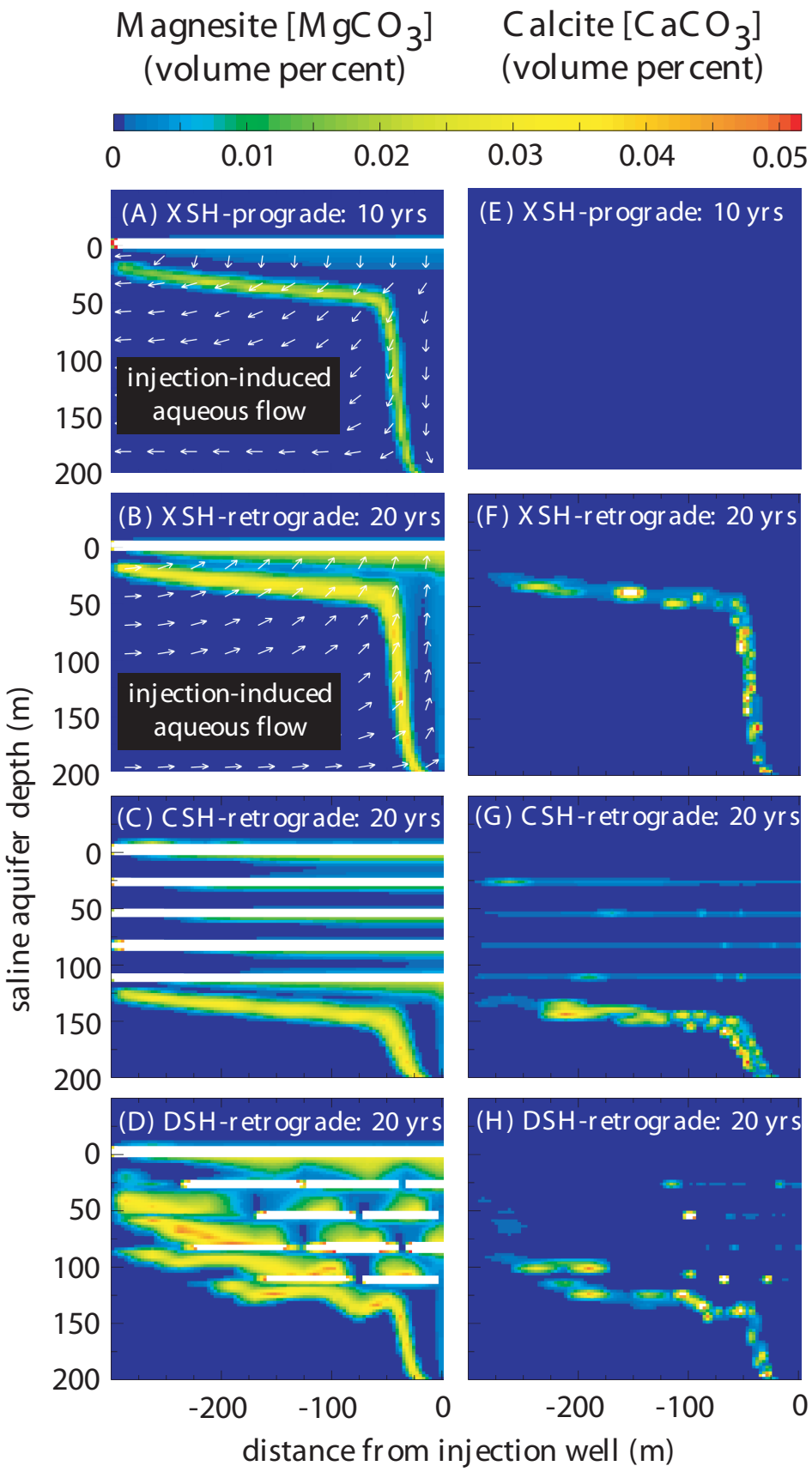
Magnesite [MgCO3] (volume percent)
Calcite [CaCO3] (volume percent)
0
0.01
0.02
0.03
0.04
0.05
(A) XSH-prograde: 10 yrs
(E) XSH-prograde: 10 yrs
injection-induced aqueous flow
(B) XSH-retrograde: 20 yrs
(F) XSH-retrograde: 20 yrs
injection-induced aqueous flow
(C) CSH-retrograde: 20 yrs
(G) CSH-retrograde: 20 yrs
(D) DSH-retrograde: 20 yrs
(H) DSH-retrograde: 20 yrs
saline aquifer depth (m)
0
50
100
150
200
-200
-100
0
distance from injection well (m)

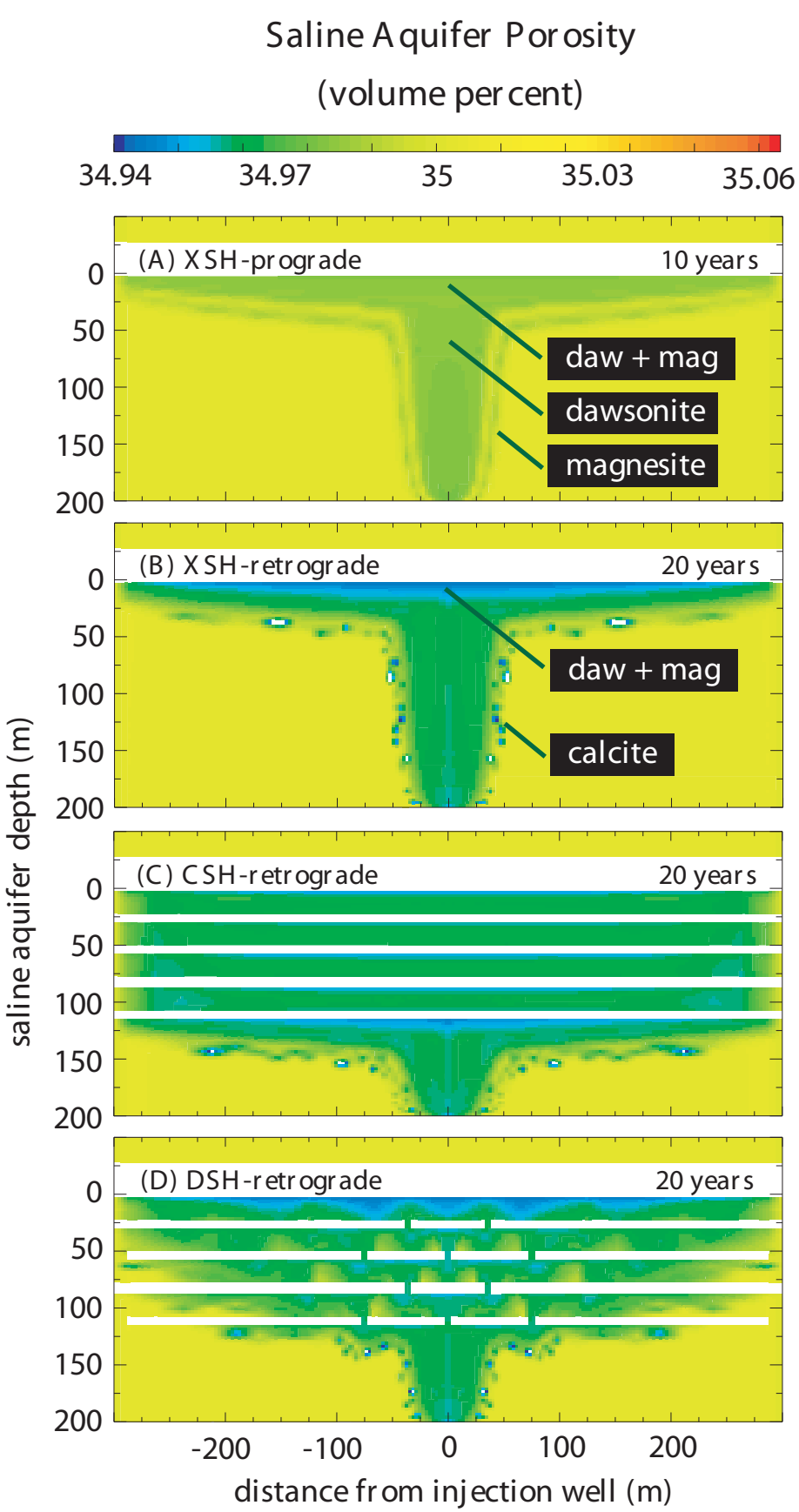
Saline Aquifer Porosity
(volume percent)
34.94
34.97
35
35.03
35.06
(A) XSH-prograde
10 years
daw + mag
dawsonite
magnesite
(B) XSH-retrograde
20 years
daw + mag
calcite
(C) CSH-retrograde
20 years
(D) DSH-retrograde
20 years
saline aquifer depth (m)
0
50
100
150
200
-200
-100
0
100
200
distance from injection well (m)

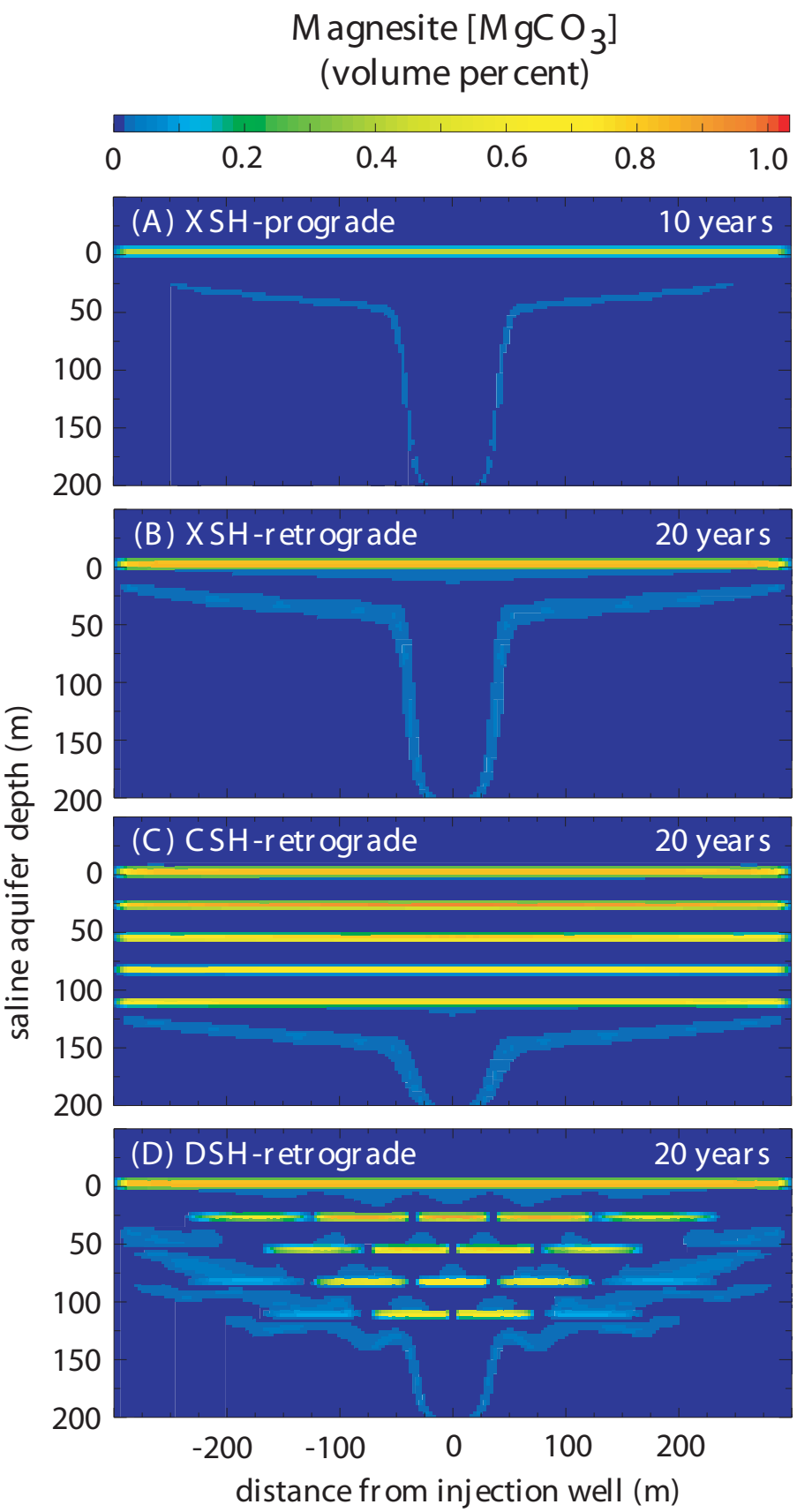
Magnesite [MgCO3]
(volume per cent)
0
0.2
0.4
0.6
0.8
1.0
(A) XSH-prograde
10 years
(B) XSH-retrograde
20 years
(C) CSH-retrograde
20 years
(D) DSH-retrograde
20 years
saline aquifer depth (m)
0
50
100
150
200
-200
-100
0
100
200
distance from injection well (m)

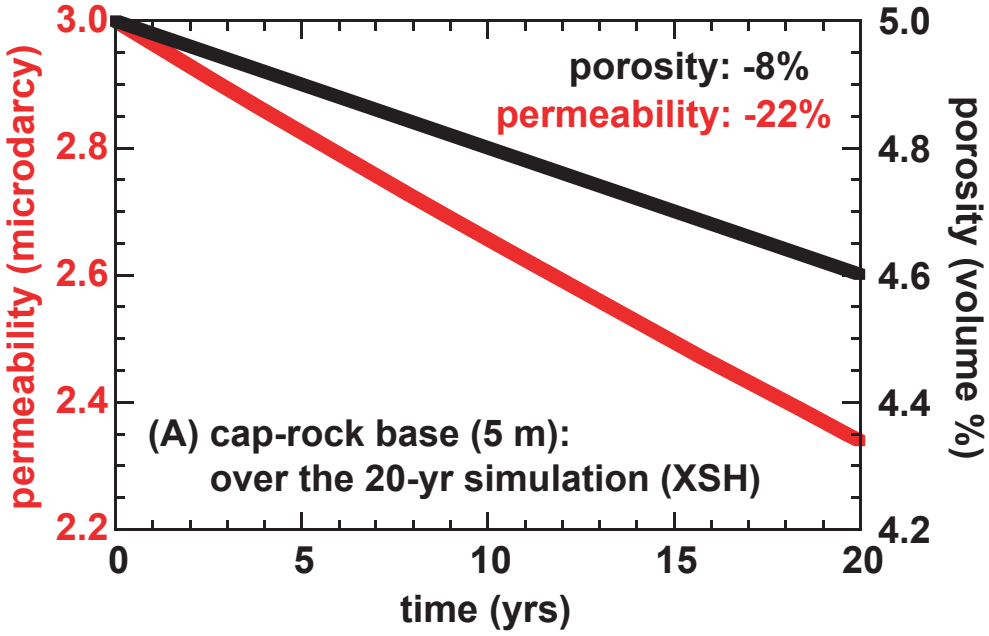
permeability (microdarcy)
porosity (volume %)
time (yrs)
porosity: -8%
permeability: -22%
(A) cap-rock base (5 m):
over the 20-yr simulation (XSH)
3.0
2.8
2.6
2.4
2.2
5.0
4.8
4.6
4.4
4.2
0
5
10
15
20

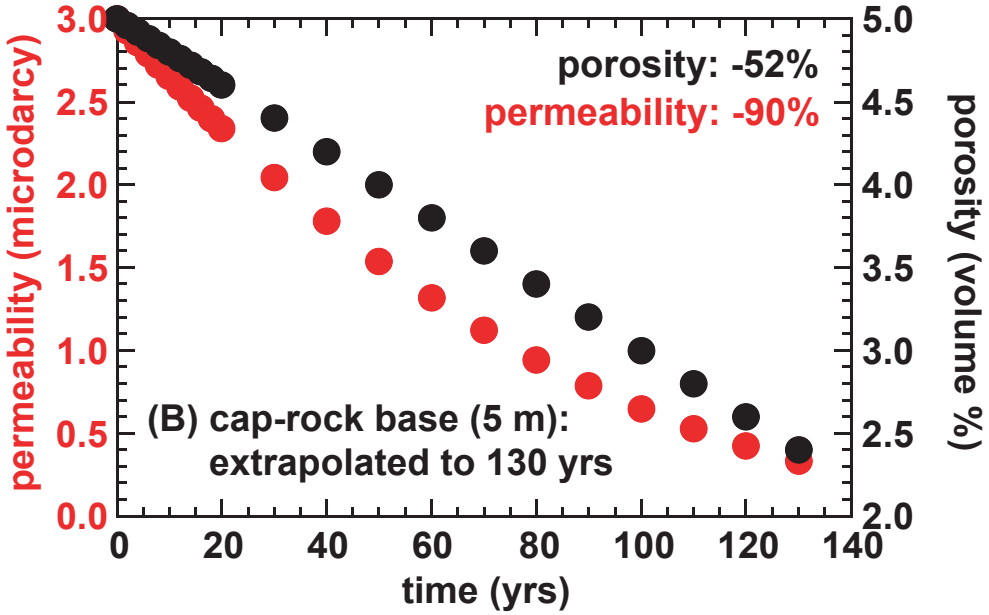
permeability (microdarcy)
porosity (volume %)
time (yrs)
porosity: -52%
permeability: -90%
(B) cap-rock base (5 m):
extrapolated to 130 yrs
3.0
2.5
2.0
1.5
1.0
0.5
0.0
5.0
4.5
4.0
3.5
3.0
2.5
2.0
0
20
40
60
80
100
120
140